

COPYRIGHTED BY

Yanglei Zou

August 2017

**I. THE FIRST MULTI-DIMENSIONAL INVERSE-SCATTERING-SERIES
INTERNAL-MULTIPLE-ELIMINATION METHOD: A NEW TOOLBOX OPTION
FOR REMOVING INTERNAL MULTIPLES THAT INTERFERE WITH A PRIMARY,
WITHOUT DAMAGING THE PRIMARY,**

AND WITHOUT ANY KNOWLEDGE OF SUBSURFACE PROPERTIES

**II. TESTS AND ANALYSIS FOR RESOLUTION COMPARISONS BETWEEN
REVERSE TIME MIGRATION (RTM) AND THE FIRST MIGRATION METHOD
THAT IS EQUALLY EFFECTIVE AT ALL FREQUENCIES AT THE TARGET**

A Dissertation presented to

the Faculty of the Department of Physics

University of Houston

In Partial Fulfillment

of the Requirements for the Degree

Doctor of Philosophy

Yanglei Zou

August 2017

I.THE FIRST MULTI-DIMENSIONAL INVERSE-SCATTERING-SERIES
INTERNAL-MULTIPLE-ELIMINATION METHOD: A NEW TOOLBOX OPTION
FOR REMOVING INTERNAL MULTIPLES THAT INTERFERE WITH A
PRIMARY, WITHOUT DAMAGING THE PRIMARY, AND WITHOUT ANY
KNOWLEDGE OF SUBSURFACE PROPERTIES

II. TESTS AND ANALYSIS FOR RESOLUTION COMPARISONS BETWEEN
REVERSE TIME MIGRATION (RTM) AND THE FIRST MIGRATION METHOD
THAT IS EQUALLY EFFECTIVE AT ALL FREQUENCIES AT THE TARGET

Yanglei Zou

APPROVED:

Dr. Arthur B. Weglein, Chairman

Dr. Nizar Chemingui

Dr. Mini Das

Dr. Fang Liu

Dr. Mark Meier

Mr. Frederico Xavier de Melo

Dr. Carlos Ordóñez

Dean, College of Natural Sciences and Mathematics

ACKNOWLEDGMENTS

The research documented in this dissertation has been carried out from summer of 2012 to summer of 2017. Firstly, I would like to especially thank Prof. Arthur B. Weglein for being my thesis advisor and supporting the project all the time. I really benefited and learned a lot from his technical knowledge, deep thoughts and communication skills. I am deeply grateful for Dr. Nizar Chemingui, Professor Mini Das, Professor Fang Liu, Professor Mark Meier, Mr. Frederico Xavier de Melo and Professor Carlos Ordonez for serving on my committee.

Meanwhile, I am grateful to my colleagues Chao Ma, Jing Wu, Xinglu Lin, Qiang Fu, Zhen Zhang, Yuchang Shen in M-OSRP who are all team-oriented and helpful. Furthermore, I would like to thank Dr. Clement Kostov for providing the opportunity of an internship in the Schlumberger and Dr. Timothy Keho for providing the opportunity of an internship in the Aramco Services Company. I also sincerely thank all my friends in both academic and industry, especially, Dr. Hyoungsu Baek, Dr. Hong Liang, Dr. James Zhiming Wu and Dr. Jingfeng Zhang. Finally, I want to express heartfelt thanks to my parents for their support and care.

CONTENTS

1. <i>Introduction</i>	1
1.1 Introduction to the first multi-dimensional ISS internal-multiple elimination method	3
1.2 Introduction to the resolution comparison between RTM and the first migration method that is equally effective at all frequencies at the target	8
2. <i>1D normal incidence ISS internal-multiple elimination algorithm</i>	14
2.1 ISS internal-multiple attenuation algorithm and the attenuation factor for 1D normal incidence	14
2.2 internal-multiple elimination algorithm	19
2.2.1 First Type of Equation Approximation for $g(z)$	22
2.2.2 Second Type of Equation Approximation for $g(z)$	22
2.2.3 Higher-order approximations and discussion	23
2.3 1D normal incidence synthetic data tests	23
2.3.1 Test for perfect data	26
2.3.2 Test for band-limited data	29
2.3.3 Test for data with noise	31

Contents

3.	<i>1D pre-stack ISS internal-multiple elimination algorithm</i>	33
3.1	A 2-reflector analytic example for the ISS internal-multiple attenuation algorithm in a 1D pre-stack acoustic medium	33
3.2	The ISS internal-multiple elimination algorithm for 1D pre-stack data	38
3.3	A numerical test for 1D pre-stack synthetic elastic PP data	39
3.4	A limitation of this elimination algorithm and an algorithm to address the limitation	42
4.	<i>Multi-dimensional acoustic ISS internal-multiple elimination algorithm</i>	43
4.1	The first Inverse-Scattering-Series internal-multiple elimination method for a multi-dimensional subsurface	43
4.2	2D acoustic synthetic data example	45
5.	<i>A Comparison of the amplitude properties of two important imaging conditions: 1 the space-time coincidence of up and down waves, and 2 the predicted coincident source and receiver experiment at depth at time zero</i>	51
5.1	Background	51
5.2	Stolt migration (Clearbout Imaging Condition III for one way wave) and Kirchhoff migration (a asymptotic form of Stolt migration)	53
5.2.1	2D Stolt migration	53
5.2.2	2D Kirchhoff migration	55
5.3	Analysis and numerical tests for the differences of Stolt migration and Kirchhoff migration due to the stationary phase approximation	57
5.3.1	Receiver side stationary phase approximation	57

Contents

5.3.2	Numerical tests	58
5.4	Obtaining the angle dependent reflection coefficient from Stolt migration and Kirchhoff migration	62
5.4.1	Obtaining the angle dependent reflection coefficient from Stolt migration	62
5.4.2	Obtaining the angle dependent reflection coefficient from kirchhoff migration	63
5.5	Conclusion	69
6.	<i>A Resolution comparison between RTM and the first migration method that is equally effective at all frequencies at the target</i>	70
6.1	Quantify the difference and impact on resolution	70
6.2	Numerical tests on a wedge model	71
7.	<i>Conclusion</i>	77
Appendix		80
A.	<i>Attenuation factor in acoustic and elastic medium</i>	81
B.	<i>Derivation of the algorithm for the elimination of all first-order internal multiples from all reflectors in a 1D medium</i>	82
C.	<i>Fourier transform of the data from the frequency-space domain to the frequency- wavenumber domain</i>	87
D.	<i>Synthetic data generation by Cagniard-de Hoop method</i>	88

<i>E. Synthetic data generation by reflectivity method</i>	89
<i>Bibliography</i>	90

ABSTRACT

The general goal of seismic exploration is to develop new capabilities in the seismic toolbox to increase our ability to locate hydrocarbons. There is a seismic processing chain of linked tasks that processes the data recorded by the receivers and produces subsurface images to serve that goal and objective. This thesis represents progress in two different links in this chain, (1) the internal-multiple removal and (2) the first migration method that is equally effective at all frequencies at the target. The organization of the thesis is as follows. First, we provide an introduction to the new internal-multiple-elimination method. Then a similar introduction is provided for the first migration method that is equally effective at all frequencies at the target. Chapters 2, 3 and 4 discuss the internal-multiple-elimination algorithm and provide numerical tests for: (1) a 1D normal incidence plane wave on an acoustic medium, (2) pre-stack 1D acoustic and elastic model data and (3) a multi-dimensional acoustic earth. Chapters 5 and 6 discuss the first migration method that is equally effective at all frequencies at the target and compare this method (for structural resolution) with current industry leading edge RTM. Chapter 7 summarizes this thesis.

1. INTRODUCTION

The objective of seismic exploration is to locate hydrocarbon (oil and gas) reservoirs in the subsurface. Figure 1.1 shows a typical marine towed streamer acquisition. A man-made source generates waves propagating in the subsurface. When the wave reaches a reflector where rock properties change, a portion of the wave is reflected upward towards the surface and then recorded by receivers. The seismic data recorded by the receivers are processed to locate subsurface interfaces (called migration/imaging) and delineate the specific earth mechanical property changes across those interfaces (called inversion). The images and material properties are important for structural interpretation and reservoir characterization.

It is useful to catalog the recorded seismic events according to their different histories, as listed below.

(1) Reference wave. Both the Inverse-Scattering-Series (ISS) method and Green's theorem method (which will be studied in this dissertation) start from perturbation theory. Perturbation theory separates the actual medium into a reference medium plus a perturbation. The choice of a reference medium depends on the specific seismic objective and application. The waves that propagate in the reference medium are called reference waves. The waves that travel in the actual medium are called the total wavefield. The difference between the total and reference waves is defined as the scattered wave (or reflection data). For marine acquisitions, if the reference medium is chosen to be a half-space of air over a half-space of

Introduction

water, the reference wave contains a direct wave¹ and wave that first travels up to the free surface² and then to the receiver. The reference wave does not experience the earth; hence, it does not carry any earth information. For land acquisitions, if the reference medium is chosen to be a homogeneous air half space over a homogeneous earth half-space, the major portion of the reference wave is the Rayleigh wave (also called ground roll). Ground roll travels along the earth's surface and causes the particles near earth's surface to move retrogradely.

(2) Ghost. Ghosts are defined after the reference wave is removed. Ghosts begin their propagation history traveling up from the source to the free surface (called source ghosts) or ending their history traveling down from the free surface to the receiver (called receiver ghosts) or both (called source-receiver ghosts).

The remaining waves that begin their history going downward from the source and end their history going upward at the receiver are further divided into primary and multiple.

(3) Multiple. A multiple experiences more than one upward reflection in its history. Multiples are further classified as free-surface multiples and internal multiples. Multiples that have at least one downward reflection at the free surface are called free-surface multiples. Multiples that have all of their downward reflections in the subsurface are called internal multiples. The order of a free-surface multiple is determined by the total number of downward reflections at the free surface. The order of an internal multiple is defined by the total number of the downward reflections that it has experienced from any subsurface reflectors (Weglein et al., 1997).

(4) Primary. A primary has only one upward reflection in its entire propagation history.

Although different types of seismic waves are recorded, the methods for extracting subsurface information from seismic data typically assume that the data consist exclusively of

¹Direct wave travels straightly from source to a receiver.

²Free surface refers to an air/water boundary for marine experiment or an air/earth boundary for onshore experiment.

Introduction

primaries (Weglein et al., 2003). There is a central and important reason for a primary-only assumption. A smooth and continuous velocity model is generally assumed in practice for different imaging methods (e.g., Claerbout (1971); Whitmore (1983); McMechan (1983); Baysal et al. (1983); Weglein et al. (2011a,b); Liu and Weglein (2014)). When a smooth and continuous velocity model is used in wave theoretic migration methods (Weglein (2014b); Weglein(2016)), primaries can be migrated to locate reflectors, whereas other waves, such as multiples, will result in false images of reflectors (Weglein, 2016). Therefore, a key goal of seismic processing, as a linked chain of steps, is to take the recorded seismic data, remove the reference waves, the ghosts and the multiples, and to output primaries.³ Figure 1.2 shows the seismic processing chain of linked tasks. Every link in the chain has seen progress in recent years. Open issues remain. This thesis represents new advances and progress in two links in this chain, the internal-multiple removal (step 4b) and the first migration method that is equally effective at all frequencies at the target (step 7a).

1.1 Introduction to the first multi-dimensional ISS internal-multiple elimination method

Multiple removal is a longstanding problem in exploration seismology. Many methods have been developed including: stacking, FK filter, Radon transform, deconvolution and Feed-back loop. They make statistical assumptions, assume move-out differences, or require knowledge of the subsurface and the generators of the multiples. As the industry trend moved to deep water and more complex on-shore and off-shore geologic plays, these methods bumped up against their assumptions, including the inability to provide adequate subsurface information.

³There are methods, e.g., Valenciano and Chemingui (2015), Lecerf et al. (2015), Lu et al. (2016) that can use multiples to enhance the image when the data has inadequate primaries. The idea and concept is to find an approximate image of an unrecorded primary, that is a subevent of the recorded multiple. However, it is always the migration of primaries that provides subsurface structure and amplitude information. (For details please see Weglein (2014b))

Introduction

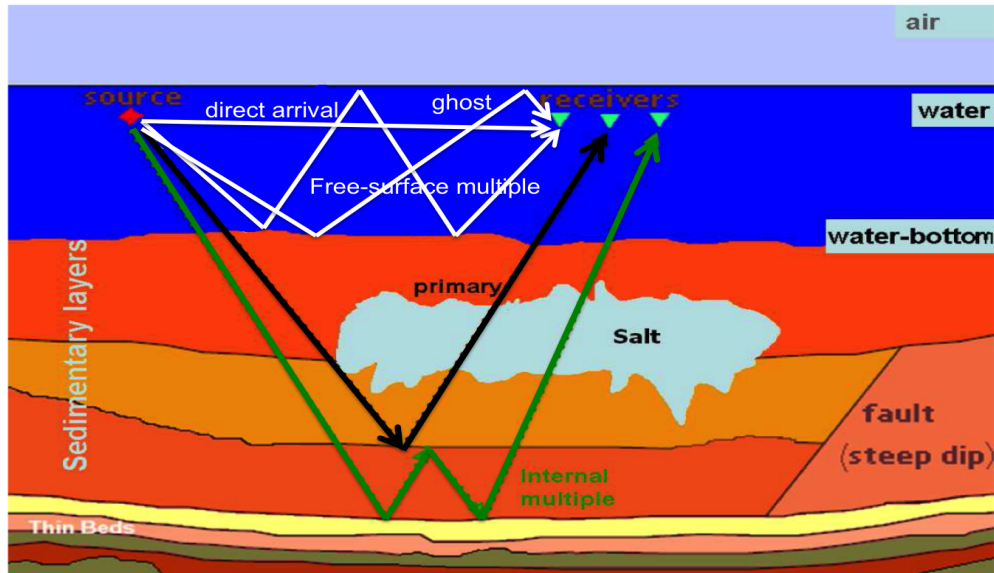


Fig. 1.1: Seismic events

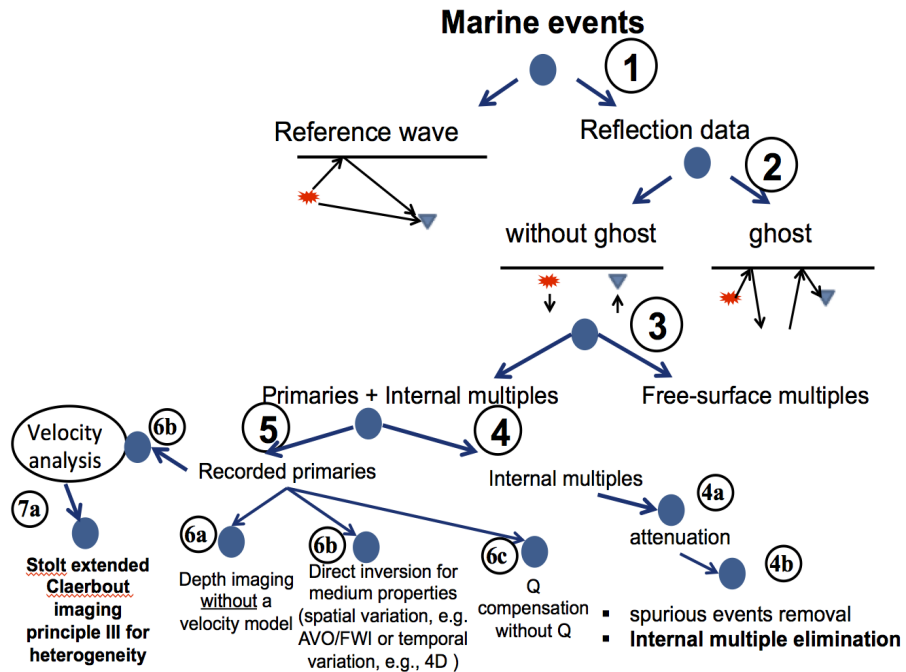


Fig. 1.2: Seismic processing chain

Introduction

The first main topic of this thesis provides the first multi-dimensional ISS internal-multiple elimination method for removing an internal multiple that interferes with a primary, without damaging the primary, and without any knowledge of subsurface properties. It assumes that before internal-multiple removal, the preprocessing steps shown in 1.2 have finished. This includes handling the non-horizontal topography of the acquisition surface (Shen and Weglein (2017), Zhang and Weglein (2017), Wu and Weglein (2017)), reference wave removal, ghost removal, and free-surface multiple removal. This method provides a new capability in the multiple-removal toolbox and a new option for circumstances when there is a high ambition and need for amplitude fidelity.

The Inverse-Scattering-Series allows all seismic processing objectives, such as free-surface-multiple removal, internal-multiple removal, depth imaging and non-linear parameter estimation to be achieved directly in terms of data, without any need to estimate or know subsurface properties.

For internal-multiple removal, the ISS internal-multiple-attenuation algorithm (Araújo et al. (1994), Weglein et al. (1997) and Weglein et al. (2003)) makes none of the assumptions of previous internal-multiple removal methods. The ISS internal-multiple-attenuation algorithm is the most capable internal-multiple removal method today used in industry and the only method that can predict the correct time and approximate and well-understood amplitude for all first-order internal multiples at once, without any subsurface information. It is especially effective when the subsurface is complicated and unknown. In order to remove multiples without damaging the primary, predicting an exact amplitude is needed. When an internal multiple is spatially and temporally separated from other events, the ISS internal-multiple-attenuation algorithm is usually combined with an energy-minimization adaptive subtraction to remove the internal multiple. For this case, the ISS internal-multiple attenuator combined with energy-minimization adaptive subtraction is often successful and effective. When internal multiples are proximal to and/or interfering with primaries or other

Introduction

events, the criteria of energy-minimization adaptive subtraction can fail (e.g., the energy can increase rather than decrease when a multiple is removed from a destructively interfering primary and multiple). With interfering events, this failure of energy-minimization adaptive subtraction can lead to removing/damaging the target primary, in exploration seismology that is the worst possible outcome.

To address this challenging problem, Weglein (2014a) proposed a three-pronged strategy:

1. Provide the prerequisites for ISS multiple removal methods for on-shore applications (e.g., removing and predicting the reference wavefield and reflection data to de-ghost the reflection data).
2. Develop internal-multiple elimination algorithms from ISS.
3. Develop a replacement for the energy-minimization criteria for adaptive subtraction that derives from and always aligns with the ISS elimination algorithm.

To the second component of this three-pronged strategy, that is, to upgrade the ISS internal-multiple attenuation algorithm to become an elimination algorithm, we begin with a review of the ISS internal-multiple-attenuation algorithm. The ISS internal-multiple-attenuation algorithm always attenuates all internal multiples from all reflectors at once, automatically and without any subsurface information. That unique strength is always present and is independent of the circumstances and complexity of the geology and the nature of the play.

The leading order term (the term used to derive the current ISS internal-multiple-attenuation algorithm) in the ISS internal-multiple-elimination sub-series, when taken in isolation, (1) may generate spurious events due to internal multiples treated as sub-events, and (2) is an attenuation algorithm not an elimination algorithm. These two aspects are anticipated and addressed by the higher-order ISS internal-multiple-removal terms. Every term in an inverse scattering task specific sub-series is specific to a certain order in the data, i.e., linear in the data, quadratic in the data, cubic in the data, etc. There is always capability

Introduction

within the overall task that the single term can achieve and there are always challenges that need the capability of the whole sub-series rather than the single term. Ma et al. (2012), H. Liang and Weglein (2012) and Ma and Weglein (2014) provide higher-order terms for spurious events removal. When taken together with the higher-order terms, the ISS internal-multiple-removal algorithm no longer experiences spurious events prediction. In a similar way, there are higher-order ISS internal-multiple removal terms that provide the capability to eliminate internal multiples, i.e., predict correct time and amplitude of internal multiples, when taken together with the leading-order attenuation term. The initial idea is provided by Weglein and Matson (1998) in which the attenuation factor, which is a collection of extra transmission coefficients and is the difference between attenuation and elimination, is systematically studied. There are further discussions in Ramírez (2007). Several extensions are proposed based on the initial idea. Herrera and Weglein (2012) proposed an internal-multiple elimination algorithm for all first-order internal multiples generated at the first reflector for 1D normal incidence. Benefiting from the above previous work, we first proposed the first-order ISS internal-multiple-elimination algorithm for 1D earth, and then developed the first multi-dimensional ISS internal-multiple elimination method that can eliminate first-order internal multiples interfering with primaries, without subsurface information, and without damaging the primaries. In the development of current elimination algorithm, we assumed an acoustic relationship $T = 1 + R$ between transmission coefficients T and reflection coefficients R. In this thesis, we provide numerical tests and analysis for both acoustic data and elastic PP data. The results demonstrate that the elimination algorithm can predict both accurate amplitude and arrival time of first-order internal multiples for acoustic data and more accurate amplitude of internal multiples than the attenuation algorithm for elastic PP data. We also compare the ISS elimination result with attenuation plus energy-minimization adaptive subtraction for an interfering primary and internal-multiple event. This ISS internal-multiple-elimination algorithm is more effective and more compute-intensive than the current most capable ISS attenuation-plus-adaptive-

Introduction

subtraction method. We provide it as a new capability in the multiple-removal toolbox as a new option for circumstances when this type of capability is called for, indicated and necessary.

In the future, we will develop a model-type independent internal-multiple elimination algorithm that can more effectively deal elastic and inelastic subsurface. We will also develop an elimination algorithm for higher-order internal multiples since they will be of a significant importance on heavily layered and strong impedance contract.

1.2 Introduction to the resolution comparison between RTM and the first migration method that is equally effective at all frequencies at the target

The second main topic of this thesis is providing a resolution comparison between RTM and the first migration method that is equally effective at all frequencies at the target.

There is an industry-wide interest in acquiring lower-frequency seismic data. There are industry reports that (1) when comparing the new and more expensively acquired broadband lower-frequency data with conventional recorded data, taken over a same region, these two data sets have the expected difference in frequency spectrum and appearance, but (2) the broadband data often provide less than the hoped for differences in structural improvement or added benefit for amplitude analysis at the target and reservoir. Weglein et al. (2016) and Fu et al. (2017) demonstrate that all current migration and migration-inversion methods make high-resolution asymptotic assumptions. Consequently, in the process of migration, they lose or discount the information in the newly acquired lowest-frequency components in the broadband data. The new Stolt extended Claerbout III migration for heterogeneous media Weglein et al. (2016) addresses this problem as the first migration method that is equally effective at all frequencies at the target and reservoir. That allows the broadband lower frequency data to provide full benefit for improving structural resolution and amplitude analysis.

Introduction

Migration methods that use wave theory for seismic imaging have two components: (1) a wave-propagation model and (2) an imaging condition. For the imaging condition component, a good start is Jon Claerbout's 1971 landmark contribution (Claerbout, 1971) which lists three imaging principles. The first is the exploding-reflector model for stacked or zero-offset data, which we call Claerbout imaging principle I (CI). The second is time-space coincidence of upgoing and downgoing waves, which we call Claerbout imaging principle II (CII). Waves propagate down from the source, are incident on the reflector, and the reflector generates a reflected upgoing wave. According to RTM (CII), the reflector exists at the location in space where the wave that is downward propagating from the source and the wave that is propagating up from the reflector are at the same place and time. The third is Claerbout imaging principle III (Stolt extended CIII), which starts with surface source and receiver data and predicts what a source and receiver would record inside the earth. Stolt extended CIII then arranges the predicted source and receiver to be coincident and asks for $t = 0$. If the predicted coincident source and receiver experiment at depth is proximal to a reflector one gets a non-zero result at time equals zero.

CII and Stolt extended CIII are of central industry interest today. Since we currently process pre-stacked data, RTM (CII) and Stolt extended CIII will produce different results.

CII can be expressed in the form

$$I(\vec{x}) = \sum_{\vec{x}_s} \sum_{\omega} S'(\vec{x}_s, \vec{x}, \omega) R(\vec{x}_s, \vec{x}, \omega), \quad (1.1)$$

where R is the reflection data running backwards in time, and S' is the complex conjugate of the source wavefield running forwards in time.

Introduction

A realization of Stolt extended CIII is Stolt FK migration (Stolt, 1978):

$$M^{stolt}(x, z) = \frac{1}{(2\pi)^3} \iiint d\omega dx_g dx_s dk_{sx} \exp(-i(k_{sz}z + k_{sx}(x - x_s))) \\ \int dk_{gx} \exp(-i(k_{gz}z + k_{gx}(x - x_s))) \int dt \exp(i\omega t) D(x_g, x_s, t). \quad (1.2)$$

The weighted sum of recorded data, summed over receivers, basically predicts the receiver experiment at depth, for a source on the surface. The sum over sources predicts the source in the subsurface. Then the predicted source and receiver experiment is the output for a coincident source and receiver, and at time equals zero; it defines a Stolt extended CIII image. Each step (integral) in this Stolt-Fourier form of Stolt extended CIII has a specific physically interpretable purpose towards the Stolt extended CIII image.

Today all migration methods assume a high-frequency approximation in a wave-propagation concept or an imaging condition or both. If you have a ray-based travel time picture of candidate images in the migration process at any step or stage in the migration method, then the migration method has made an asymptotic high-frequency assumption/approximation (see figure 1.3). As we will see for RTM (CII), for one source and one receiver, the image is an ellipse. If you have a travel-time ellipse of candidate images, that is an absolute indicator that the migration method has made a high-frequency approximation.

In figures 1.4 and 1.5, we compare the results of RTM (CII) and Stolt extended CIII for one source and one receiver. RTM (CII) provides an ellipse while Stolt extended CIII does not. Stolt extended CIII provides a local image. For RTM (CII), in this simplest case, where the data is perfect and the medium is homogeneous, the contribution from one source and one receiver yields a set of candidates. Stolt extended CIII will never provide candidates. Stolt extended CIII will bring you to a point in the earth where you have a coincident source and receiver experiment. At time equals zero, if there is a non zero result, you are at a reflector. There is structure there, not a possible or candidate structure. The result from RTM (CII)

Introduction

is a set of candidates of possible structure. That is intrinsic to CII, hence intrinsic to all current RTM. Hence, if you are imaging with RTM or any extension of RTM, it is worth noting that you have made a high-frequency approximation in your migration methods.

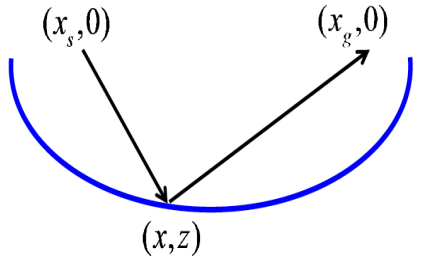


Fig. 1.3: For example, if within a migration method, and focusing on the output of a single trace for a source at $(x_s, 0)$ and a receiver at $(x_g, 0)$ above a single reflector produces a single event that will arrive at time, t_1 . If the migration method outputs a "ray theory" high frequency approximation for a single event at time t_1 , it will become a set of candidate points (x, y) where $\frac{r_s + r_g}{t_1} = C_0$ where $r_s = \sqrt{(x - x_s)^2 + (y - y_s)^2}$ and $r_g = \sqrt{(x - x_g)^2 + (y - y_g)^2}$

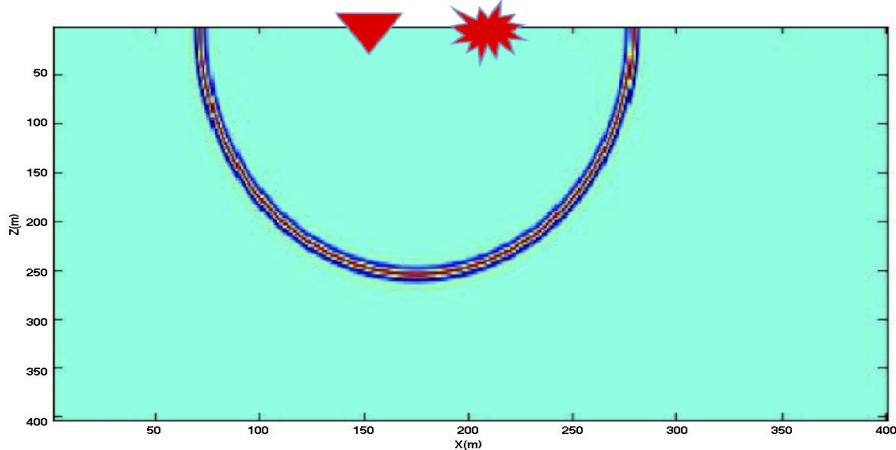


Fig. 1.4: 2D RTM (CII) result for one source and one receiver. There is an intrinsic high frequency assumption within the RTM (CII) imaging principle

All RTM (CII) imaging, i.e., all RTM methods in use today, incorporate high-frequency approximations/assumptions in the imaging principle itself, regardless of how they are implemented. For a heterogeneous medium and assuming one-way propagation (at a point, or overall downgoing between source and reflector and then upgoing from reflector to receiver),

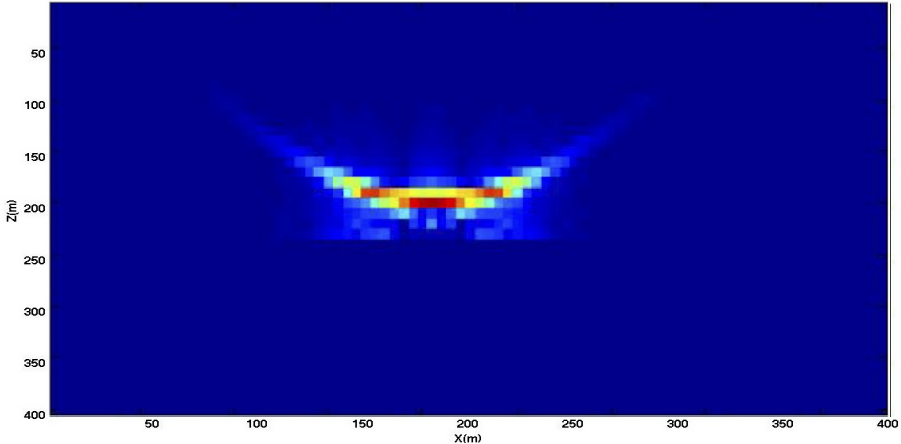


Fig. 1.5: 2D Stolt extended CIII Stolt migration result for one source and one receiver. No high frequency assumption is within the Stolt extended CIII imaging principle

a high-frequency approximation has been made, even if you are adopting a CIII imaging principle.

Equation 1.3 is the new Stolt extended CIII migration method for heterogeneous media in Weglein et al. (2016).

$$P = \int_{S_s} \left[\frac{\partial G_0^{DN}}{\partial z_s} \int_{S_g} \left\{ \frac{\partial G_0^{DN}}{\partial z_g} P + \frac{\partial P}{\partial z_g} G_0^{DN} \right\} dS_g + G_0^{DN} \frac{\partial}{\partial z_s} \int_{S_g} \left\{ \frac{\partial G_0^{DN}}{\partial z_g} P + \frac{\partial P}{\partial z_g} G_0^{DN} \right\} dS_g \right] dS_s \quad (1.3)$$

Equation 1.3 was Stolt extended CIII imaging for a heterogeneous medium, and doesn't assume one-way propagation at either a point, or, separately, overall between source and reflector, and, reflector to receiver. G_0^{DN} is the Green's function for the heterogeneous medium that vanishes along with its normal derivative at the lower surface of the migration volume (Weglein et al., 2011b). Equation 1.3 is the first migration method that makes no high-frequency approximation in both wave-propagation concept and in the imaging condition for heterogeneous media, i.e., it is equally effective at all frequencies at the target and at the reservoir. For details please see Weglein et al. (2011a;b) and F. Liu and Weglein

Introduction

(2014).

In this thesis, we focus on the comparison for structural resolution between RTM (CII) and CIII. Fu et al. (2017) provides the first quantification of the side lobe difference and impact on resolution for RTM (CII) and Stolt extended CIII for a single reflector. We continue to study and quantify these differences in the migration resolution using a wedge model and define the added resolution value provided by the new Stolt extended CIII migration for a heterogeneous medium. The side lobes of the images of upper and lower reflectors produce an interference that determines resolution. The migration method with a greater reduction of side lobes will be the migration with a greater ability to resolve two reflectors with the same bandwidth in the data, conventional or band limited.

2. 1D NORMAL INCIDENCE ISS INTERNAL-MULTIPLE ELIMINATION ALGORITHM

2.1 ISS internal-multiple attenuation algorithm and the attenuation factor for 1D normal incidence

The ISS internal-multiple attenuation algorithm is first given by Araújo (1994) Weglein et al. (1997). The 1D normal incidence version of the algorithm is presented as follows:

$$b_3^{IM}(k) = \int_{-\infty}^{\infty} dz e^{ikz} b_1(z) \int_{-\infty}^{z-\varepsilon_2} dz' e^{-ikz'} b_1(z') \int_{z'+\varepsilon_1}^{\infty} dz'' e^{ikz''} b_1(z''). \quad (2.1)$$

Where $b_1(z)$ is the water speed migration of the data due to a 1D normal incidence spike plane wave. In the following example, we will show how to obtain $b_1(z)$ from data. $b_3^{IM}(k)$ is the predicted internal multiples in the frequency domain. ε_1 and ε_2 are two small positive number introduced to define resolution. This equation can predict the correct time and approximate amplitude of all first-order internal multiples.

To demonstrate explicitly the mechanism of the ISS internal-multiple attenuation algorithm and to examine its properties, Weglein et al. (2003) considered the simplest two-layer model (figure 2.1) that can produce an internal multiple. For this model, the reflection data caused by an impulsive incident wave $\delta(t - \frac{z}{c})$ is:

$$D(t) = R_1 \delta(t - t_1) + T_{01} R_2 T_{10} \delta(t - t_2) - R_1 R_2^2 T_{01} T_{10} \delta(t - (2t_2 - t_1)) \dots \quad (2.2)$$

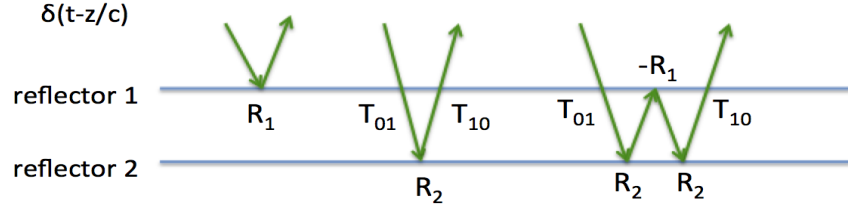


Fig. 2.1: two-layer model

where t_1 , t_2 and R_1 , R_2 are the two way times and reflection coefficients from the two reflectors, respectively; T_{01} and T_{10} are the coefficients of transmission between model layers 0 and 1 and 1 and 0, respectively.

$$D(\omega) = R_1 e^{i\omega t_1} + T_{01} R_2 T_{10} e^{i\omega t_2} - R_1 R_2^2 T_{01} T_{10} e^{i\omega(2t_2-t_1)} \dots \quad (2.3)$$

where $D(\omega)$ is the temporal fourier transform of $D(t)$.

Given a 1D medium and a normal incident wave, we have $k_z = \frac{2\omega}{c_0}$ and $b_1(k_z) = D(\omega)$. The following is obtained:

$$b_1(k_z) = R_1 e^{ik_z \frac{c_0 t_1}{2}} + T_{01} R_2 T_{10} e^{ik_z \frac{c_0 t_2}{2}} - R_1 R_2^2 T_{01} T_{10} e^{ik_z \frac{c_0(2t_2-t_1)}{2}} \dots \quad (2.4)$$

The pseudo-depths z_1 and z_2 in the reference medium are defined as follows:

$$z_1 = \frac{c_0 t_1}{2} \quad z_2 = \frac{c_0 t_2}{2}. \quad (2.5)$$

The input data can now be expressed in terms of $k = k_z$, z_1 and z_2 :

$$b_1(k) = R_1 e^{ik z_1} + T_{01} R_2 T_{10} e^{ik z_2} - R_1 R_2^2 T_{01} T_{10} e^{ik(2z_2-z_1)} \dots \quad (2.6)$$

The data is now ready for the internal-multiple attenuation algorithm.

Substituting $b_1(k)$ into the algorithm (equation 2.1), we derive the prediction:

$$b_3^{IM}(k) = R_1 R_2^2 T_{01}^2 T_{10}^2 e^{2ikz_2} e^{-ikz_1} \quad (2.7)$$

which in the time domain is:

$$b_3^{IM}(t) = R_1 R_2^2 T_{01}^2 T_{10}^2 \delta(t - (2t_2 - t_1)) \quad (2.8)$$

The actual first-order internal multiple in the data is:

$$-R_1 R_2^2 T_{01} T_{10} \delta(t - (2t_2 - t_1)) \quad (2.9)$$

Therefore, the time prediction is precise, and the amplitude of the prediction has an extra power of $T_{01} T_{10}$ which is called the attenuation factor, thus defining exactly the difference between the attenuation(represented by b_3^{IM}) and elimination.

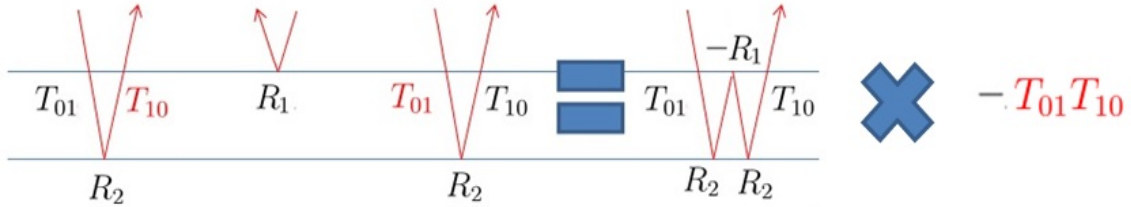


Fig. 2.2: an example of the attenuation factor of a first-order internal multiple generated at the shallowest reflector, notice that all red terms are extra transmission coefficients

The procedure of predicting a first-order internal multiple generated at the shallowest reflector is shown in figure 2.2. The ISS internal-multiple attenuation algorithm automatically combines three primary sub-events in the data to predict a first-order internal multiple. The amplitude of the predicted internal multiple is the multiplication of the sub-event amplitude. The predicted time is the sum of the arrival time of the two deeper sub-events minus the arrival time of the shallower sub-event. When compared with the internal mul-

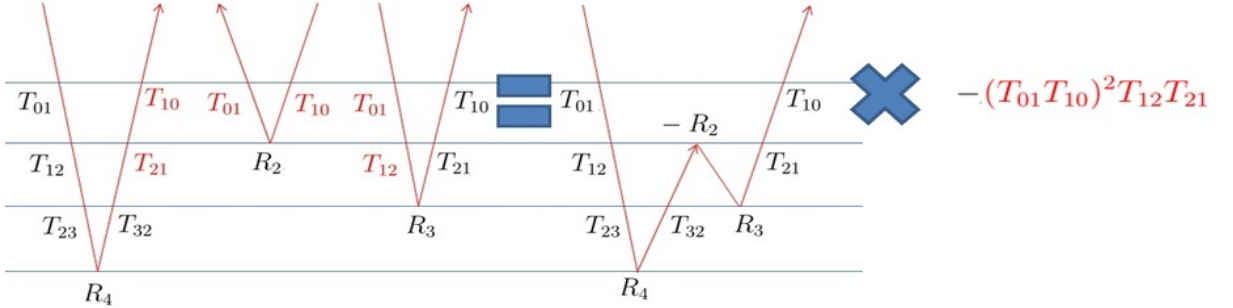


Fig. 2.3: an example of the attenuation factor of a first-order internal multiple generated at the next shallowest reflector, notice that all red terms are extra transmission coefficients

tiple on the right hand side, the sub-events on the left hand side have extra transmission coefficients as shown in red. Multiplying all those extra transmission coefficients, we get the attenuation factor $T_{01}T_{10}$ for this first-order internal multiples generated at the shallowest reflector. All first-order internal multiples generated at the shallowest reflector have the same attenuation factor.

Figure 2.3 shows the procedure of predicting a first-order internal multiple generated at the next shallowest reflector. In this case, the attenuation factor is $(T_{01}T_{10})^2(T_{12}T_{21})$.

To derive a general formula for the amplitude prediction of the algorithm, Ramírez (2007) analyzed a model with n layers and respective velocities C_n , n is an integer. By using the definitions $R_1 = R'_1$, $R'_N = R_N \prod_{i=1}^{N-1} (T_{i-1,i} T_{i,i-1})$ and Einstein's summation, the reflection data from a normal incident spike wave we obtain the following:

$$D(t) = R'_n \delta(t - t_n) + \text{internal multiples} \quad (2.10)$$

The generalized prediction of the attenuation algorithm is obtained by the following:

$$b_3^{IM}(k) = R'_i R'_j R'_k e^{ikz_i} e^{ikz_j} e^{ikz_k} \quad (2.11)$$

which in the time domain becomes

$$b_3^{IM}(t) = R'_i R'_j R'_k \delta(t - (t_i + t_k - t_j)) \quad (2.12)$$

By evaluating equation (2.11) for different values of i, j and k the amplitude prediction of first-order internal multiples is obtained and can be generalized for any amount of layers in a 1D model. The generalization of the internal multiple amplitude states that the over-abundance of transmission coefficients depends on the position of the generating reflector (where the downward reflection took place). Compared with the real amplitude of internal multiples in the data, we can obtain the attenuation factor.

The attenuation factor, AF_j , in the prediction of internal multiples is given by the following:

$$AF_j = \begin{cases} T_{0,1}T_{1,0} & (\text{for } j = 1) \\ \prod_{i=1}^{j-1} (T_{i-1,i}^2 T_{i,i-1}^2) T_{j,j-1} T_{j-1,j} & (\text{for } 1 < j < J) \end{cases} \quad (2.13)$$

The attenuation factor AF_j can also be performed by using reflection coefficients:

$$AF_j = \begin{cases} 1 - R_1^2 & (\text{for } j = 1) \\ (1 - R_1^2)^2 (1 - R_2^2)^2 \cdots (1 - R_{j-1}^2)^2 (1 - R_j^2) & (\text{for } 1 < j < J) \end{cases} \quad (2.14)$$

The subscript j represents the generating reflector, and J is the total number of interfaces in the model. The interfaces are numbered starting with the shallowest location. The attenuation algorithm b_3^{IM} predicts a first-order internal multiple by using three events within the data. The attenuation factor is directly related to the trajectory of the events, which forms the prediction of the internal multiple.

2.2 internal-multiple elimination algorithm

The discussion in the previous section demonstrates that all first-order internal multiples generated at the same reflector have the same attenuation factor and internal multiples generated at different reflectors have different attenuation factors. We also derived a generalized formula for the attenuation factor for all reflectors. We can see the attenuation factor contains all transmission coefficients from the shallowest reflector down to the reflector generating the multiple. And from the examples(shown in figure 2.2 and 2.3) we can see the middle event contains all those transmission coefficients. Therefore, our idea is to modify the middle term in the attenuation algorithm to remove the attenuation factor and turn the attenuation algorithm into an elimination algorithm. That is from

$$b_3^{IM}(k) = \int_{-\infty}^{\infty} dz e^{ikz} b_1(z) \int_{-\infty}^{z-\varepsilon_2} dz' e^{-ikz'} b_1(z') \int_{z'+\varepsilon_1}^{\infty} dz'' e^{ikz''} b_1(z'') \quad (2.15)$$

to

$$b_E^{IM}(k) = \int_{-\infty}^{\infty} dz e^{ikz} b_1(z) \int_{-\infty}^{z-\varepsilon_2} dz' e^{-ikz'} \mathbf{F}[b_1(z')] \int_{z'+\varepsilon_1}^{\infty} dz'' e^{ikz''} b_1(z'') \quad (2.16)$$

For the 1D normal incidence, $b_1(z)$ is expressed as follows:

$$b_1(z) = R_1 \delta(z - z_1) + R'_2 \delta(z - z_2) + R'_3 \delta(z - z_3) + \cdots + R'_n \delta(z - z_n) + \cdots \quad (2.17)$$

To remove all attenuation factor in the prediction, the $\mathbf{F}[b_1(z)]$ should be written as the

following:

$$\begin{aligned}
 F[b_1(z')] &= \frac{R_1}{AF_{j=1}} \delta(z' - z_1) + \frac{R'_2}{AF_{j=2}} \delta(z' - z_2) + \cdots + \frac{R'_n}{AF_{j=n}} \delta(z' - z_n) + \cdots \\
 &= \frac{R_1}{1 - R_1^2} \delta(z' - z_1) + \frac{R'_2}{(1 - R_1^2)^2 (1 - R_2^2)} \delta(z' - z_2) + \cdots \\
 &\quad + \frac{R'_n}{(1 - R_1^2)^2 (1 - R_2^2)^2 \cdots (1 - R_{n-1}^2)^2 (1 - R_n^2)} \delta(z' - z_n) + \cdots
 \end{aligned} \tag{2.18}$$

Here we use the relationship $T=1+R$ between transmission coefficient T and reflection coefficient R . This relationship is valid only in acoustic medium. For elastic medium it is an approximation. In appendix A, we have more detailed discussion on this topic.

The basic strategy to construct $F[b_1(z)]$ in terms of $b_1(z)$ is to first construct the attenuation factor by $b_1(z)$, then construct $F[b_1(z)]$ using $b_1(z)$ and attenuation factor. The attenuation factor can be written in transmission coefficients, and then reflection coefficients, and map the reflection coefficients to R' 's (R' 's are the amplitude of the events in data), finally construct these R' 's by $b_1(z)$, as shown in figure 2.4. However, we tried this way and found out it is difficult to achieve.

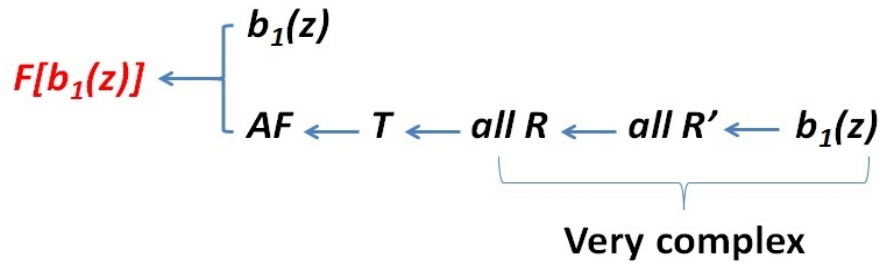


Fig. 2.4: The straight forward strategy

Then we proposed another way to achieve the goal. By introducing a new function called $g(z)$ in which the amplitude of each event corresponds to a reflection coefficient, we find a way to construct $F[b_1(z)]$ by using $b_1(z)$ and $g(z)$. After that, we find an integral equation

about $b_1(z)$ and $g(z)$. If we can solve the latter equation for $g(z)$ and integrate it into the first part, we can achieve our goal(shown in figure 2.5).

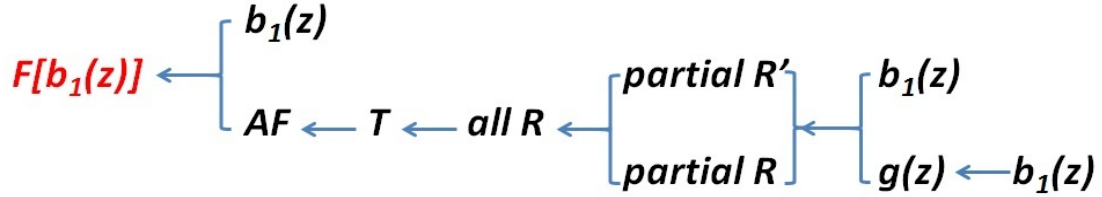


Fig. 2.5: Modified strategy

By using that modified strategy, the $F[b_1(z)]$ is discovered (See appendix B for the derivation):

$$F[b_1(z)] = \frac{b_1(z)}{\left[1 - (\int_{z-\varepsilon}^{z+\varepsilon} dz' g(z'))^2\right]\left[1 - \int_{-\infty}^{z-\varepsilon} dz' b_1(z') \int_{z'-\varepsilon}^{z'+\varepsilon} dz'' g(z'')\right]^2} \quad (2.19)$$

$$g(z) = \frac{b_1(z)}{1 - \int_{-\infty}^{z-\varepsilon} dz' b_1(z') \int_{z'-\varepsilon}^{z'+\varepsilon} dz'' g(z'')} \quad (2.20)$$

To derive the $F[b_1(z)]$ from $b_1(z)$, $g(z)$ must first be solved in equation (2.20). Thereafter, $g(z)$ is integrated into equation (2.19).

Equation (2.20) is an integral equation. Generally speaking, this kind of equation does not have analytical solutions; hence, an approximation must be made to solve this equation.

2.2.1 First Type of Equation Approximation for $g(z)$

The simplest approximation for $g(z)$ is presented as follows:

$$\begin{aligned} g(z) &= \frac{b_1(z)}{1 - \int_{-\infty}^{z-\varepsilon} dz' b_1(z') \int_{z'-\varepsilon}^{z'+\varepsilon} dz'' g(z'')} \\ &\approx \frac{b_1(z)}{1 - 0} \\ &\approx b_1(z) \end{aligned} \quad (2.21)$$

It can be shown that substituting this type of approximation of $g(z)$ to $F[b_1(z)]$, the algorithm can predict correct amplitude for all 1st order internal multiples generated at the shallowest reflector and can further attenuate deeper internal multiples.

2.2.2 Second Type of Equation Approximation for $g(z)$

A more accurate approximation for $g(z)$ is presented as follows::

$$\begin{aligned} g(z) &= \frac{b_1(z)}{1 - \int_{-\infty}^{z-\varepsilon} dz' b_1(z') \int_{z'-\varepsilon}^{z'+\varepsilon} dz'' \textcolor{red}{g}(z'')} \\ &\approx \frac{b_1(z)}{1 - \int_{-\infty}^{z-\varepsilon} dz' b_1(z') \int_{z'-\varepsilon}^{z'+\varepsilon} dz'' \textcolor{red}{b}_1(z'')} \end{aligned} \quad (2.22)$$

Substituting this type of approximation of $g(z)$ to $F[b_1(z)]$, the algorithm can predict the correct amplitude for all first-order internal multiples generated at the shallowest and next shallowest reflectors and can further attenuate deeper internal multiples.

2.2.3 Higher-order approximations and discussion

By iterating $g(z)$ in (2.20), we can get a more accurate approximation, as shown in figure 2.6. Substitute more accurate approximations of $g(z)$ into $F[b_1(z)]$, we will get higher orders of approximation of the elimination algorithm which can predict correct amplitude of first-order internal multiples generated at deeper reflectors.

However, when predicting first-order internal multiples generated at deeper reflectors using further approximations, there is an issue caused by the multiples in the input. To deal with this issue, we can first apply the ISS internal-multiple attenuation algorithm, then attenuate the internal multiples in the data and then apply this new elimination algorithm using the new data to eliminate all first-order internal multiples.

2.3 1D normal incidence synthetic data tests

This section presents initial tests that shows the result of the original ISS internal-multiple attenuation algorithm and two different types of equation approximation of the elimination algorithm. Figure 2.7 and 2.8 show the model used in this study and the 1D normal incidence input data, respectively. In figure 2.8, the part in the red rectangular shows the part of data that we focus on.

First type approximation for equation(6)	$g(z) = \frac{b_1(z)}{1 - \int_{-\infty}^{z-\varepsilon} dz' b_1(z') \int_{z'-\varepsilon}^{z'+\varepsilon} dz'' g(z'')}$ $\approx \frac{b_1(z)}{1 - 0}$ $\approx b_1(z)$
Second type approximation for equation(6)	$g(z) = \frac{b_1(z)}{1 - \int_{-\infty}^{z-\varepsilon} dz' b_1(z') \int_{z'-\varepsilon}^{z'+\varepsilon} dz'' \mathbf{g}(z'')}$ $\approx \frac{b_1(z)}{1 - \int_{-\infty}^{z-\varepsilon} dz' b_1(z') \int_{z'-\varepsilon}^{z'+\varepsilon} dz'' \mathbf{b}_1(z'')}$
Third type approximation for equation(6)	$g(z) = \frac{b_1(z)}{1 - \int_{-\infty}^{z-\varepsilon} dz' b_1(z') \int_{z'-\varepsilon}^{z'+\varepsilon} dz'' \mathbf{g}(z'')}$ $\approx \frac{b_1(z)}{1 - \int_{-\infty}^{z-\varepsilon} dz' b_1(z') \int_{z'-\varepsilon}^{z'+\varepsilon} dz'' \frac{b_1(z'')}{1 - \int_{-\infty}^{z''-\varepsilon} dz''' b_1(z''') \int_{z'''-\varepsilon}^{z'''+\varepsilon} dz^{(4)} b_1(z^{(4)})}}$

Fig. 2.6: different approximations for $g(z)$

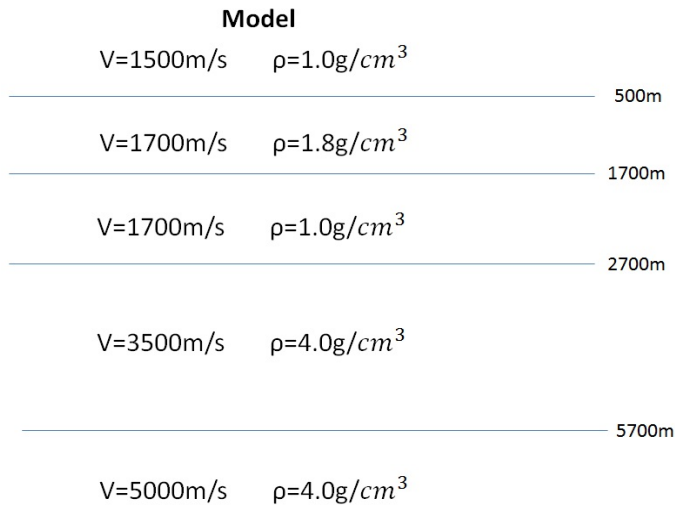


Fig. 2.7: Model

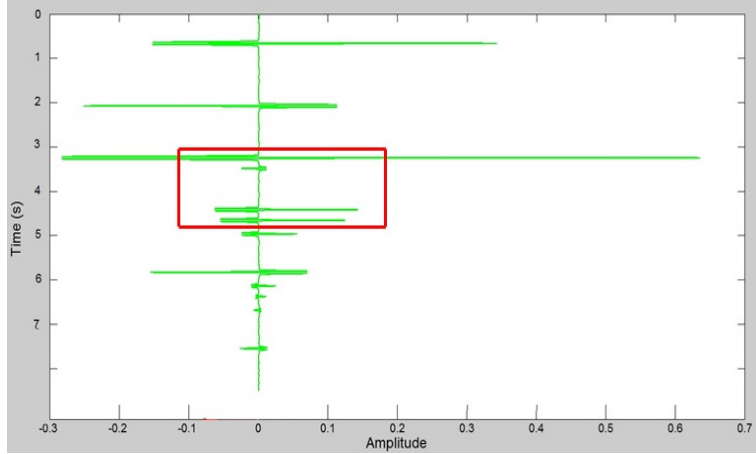


Fig. 2.8: Input data (The amplitude does not have units.)

2.3.1 Test for perfect data

With perfect data¹, the output of ISS internal-multiple attenuation algorithm in figure 2.9² clearly shows that all multiples are predicted with the correct time and approximate amplitude. Figure 2.10, which displays the first type of equation approximation, shows that all internal multiples with a downward reflection at the shallowest reflector(IM_{212}, IM_{312} and IM_{213})are removed and other internal multiples generated by deeper reflectors are further attenuated. And in Figure 2.11,we can see all internal multiples generated at the shallowest and the next shallowest reflectors($IM_{212}, IM_{312}, IM_{213}$ and IM_{323}) are removed by the second type of equation approximation.

¹Perfect data means the data is full bandwidth and noise free.

²In These figures: P_3 is the Third primary. $IM_{212}, IM_{213}, IM_{312}$ are internal multiples with a downward reflection at the shallowest reflector.The three numbers in the subscript refer to the historical number of reflectors in the internal multiples. For example, IM_{212} is a first-order internal multiple with two upward reflection at the second reflector and a downward reflection at the first(shallowest) reflector. IM_{323} is a first-order internal multiple with a downward reflection at the next shallowest reflector. The spurious event is an false event generated by IM_{212}, P_3 and IM_{212} , which exist in every figure. A algorithm for removing the spurious events have been discovered by Ma et al. (2012) H. Liang and Weglein (2012).

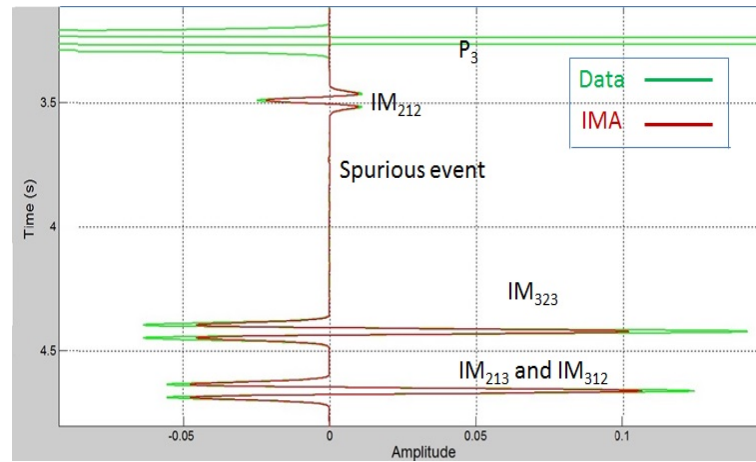


Fig. 2.9: Output of the ISS internal-multiple attenuation algorithm (The amplitude does not have units.)

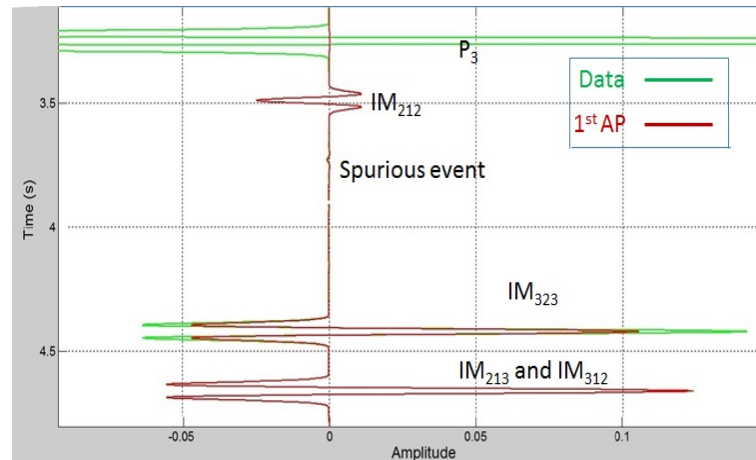


Fig. 2.10: Output of the first type of equation approximation (The amplitude does not have units.)

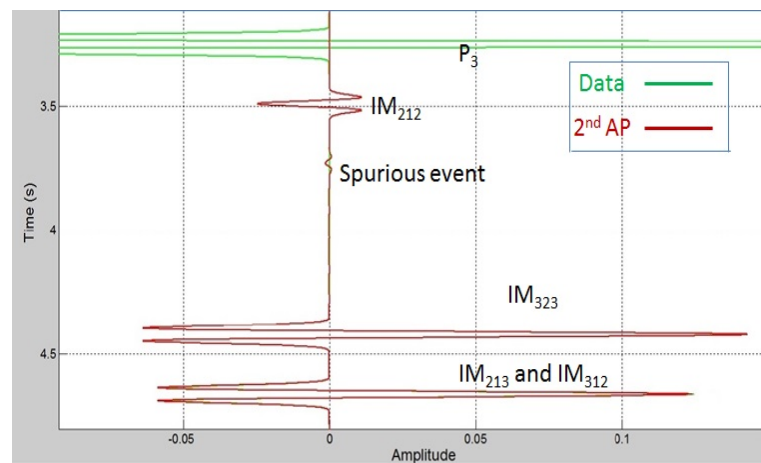


Fig. 2.11: Output of the second type of equation approximation (The amplitude does not have units.)

2.3.2 Test for band-limited data

The second test is using band-limited data as input. As shown in figure 2.12, the attenuation algorithm is almost immune to bandwidth. In figure 2.13 and 2.14, we can see the elimination algorithm can still further attenuate multiples for band-limited data, although with some errors.

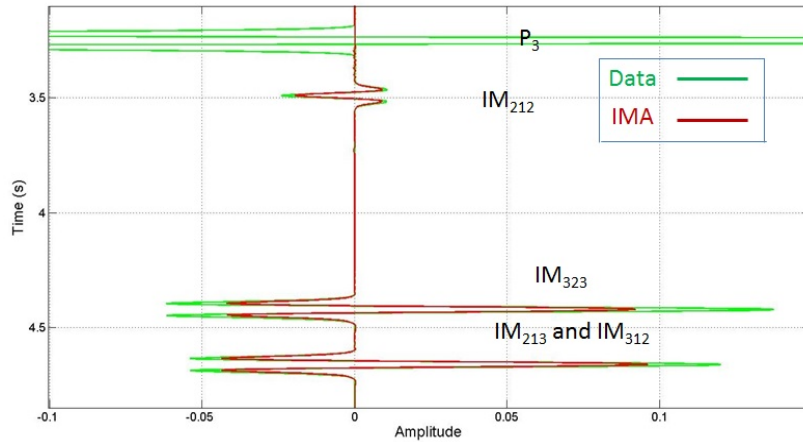


Fig. 2.12: Output of the ISS internal-multiple attenuation algorithm for bandlimited data (The amplitude does not have units.)

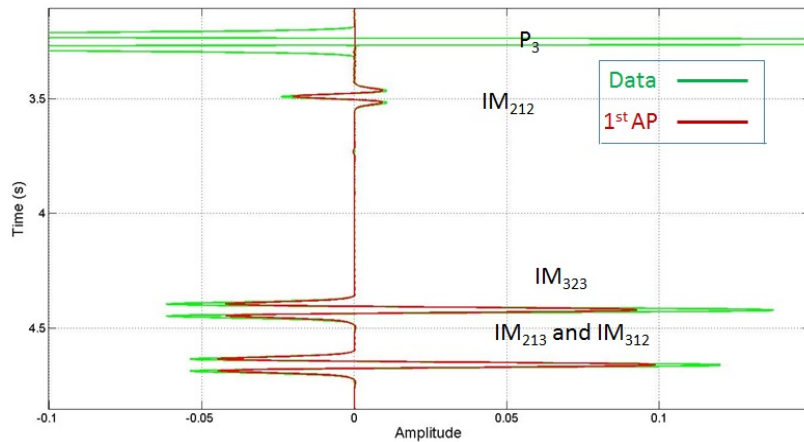


Fig. 2.13: Output of the first type of equation approximation for bandlimited data (The amplitude does not have units.)

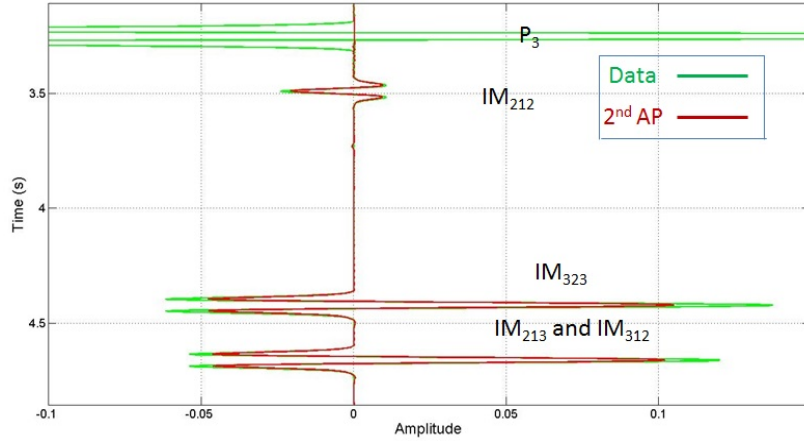


Fig. 2.14: Output of the second type of equation approximation for bandlimited data (The amplitude does not have units.)

2.3.3 Test for data with noise

The third test is using data with noise as input. As shown in figure 2.15, 2.16, 2.17, both attenuation and elimination algorithm are almost immune to noise, with very encouraging result.

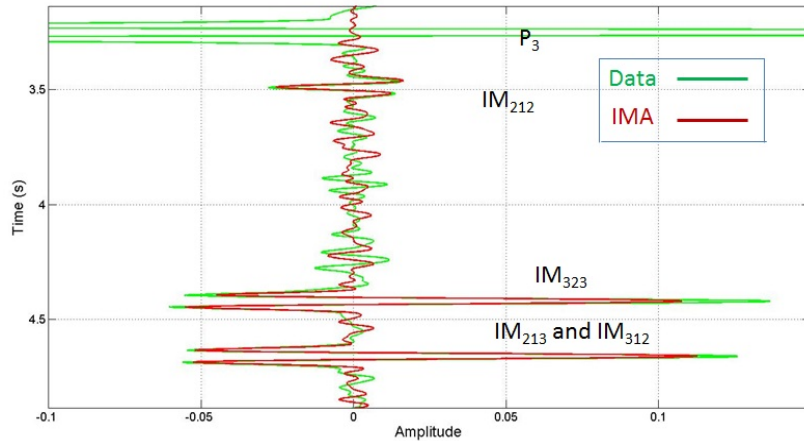


Fig. 2.15: Output of the ISS internal-multiple attenuation algorithm for data with noise (The amplitude does not have units.)

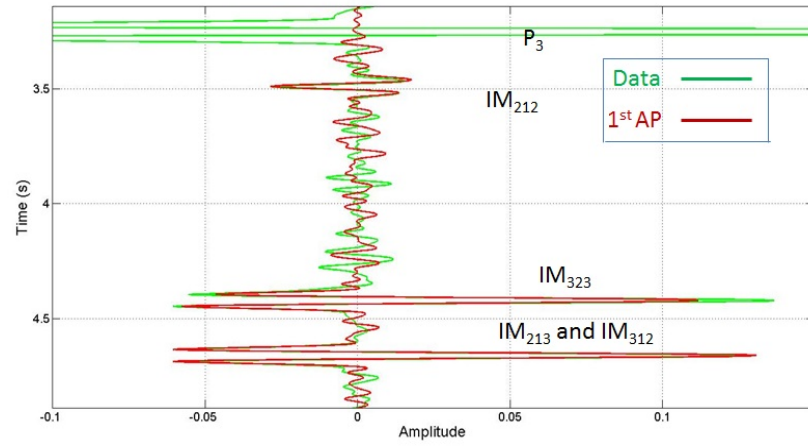


Fig. 2.16: Output of the first type of equation approximation for data with noise (The amplitude does not have units.)

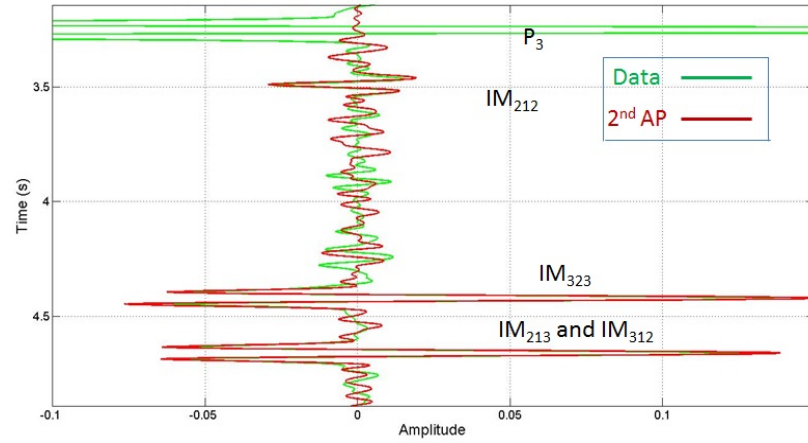


Fig. 2.17: Output of the second type of equation approximation for data with noise (The amplitude does not have units.)

3. 1D PRE-STACK ISS INTERNAL-MULTIPLE ELIMINATION ALGORITHM

3.1 A 2-reflector analytic example for the ISS internal-multiple attenuation algorithm in a 1D pre-stack acoustic medium

In this section, we discuss a 2-reflector analytic example in a 1D pre-stack acoustic medium. First we calculate the analytic data. Considering a delta source at (x_s, z_s) , the wave generated at (x_g, z_g) by this source is (the Green's function):

$$G_0(x_g, z_g, x_s, z_s, \omega) = \frac{1}{2\pi} \int_{-\infty}^{\infty} dk'_s \frac{e^{ik'_s(x_g-x_s)} e^{iq'_s|z_g-z_s|}}{2iq'_s} \quad (3.1)$$

Let us set $z_s = 0$ and let z_g be positive, so that we can evaluate the absolute value in the integrand,

$$G_0(x_g, z_g > 0, x_s, z_s = 0, \omega) = \frac{1}{2\pi} \int_{-\infty}^{\infty} dk'_s \frac{e^{-ik'_s x_s}}{2iq'_s} e^{ik'_s x_g + iq'_s z_g}. \quad (3.2)$$

Then, for simplicity, the evanescent part is ignored, which means $k'_s < \omega/c$. That does not mean the algorithm can not handle the evanescent part. However, for many cases the evanescent part is small and can be ignored, and the math will be much simpler and easier to understand. Now the Green's function is:

$$G_0(x_g, z_g > 0, x_s, z_s = 0, \omega) = \frac{1}{2\pi} \int_{-\omega/c}^{\omega/c} dk'_s \frac{e^{-ik'_s x_s}}{2iq'_s} e^{ik'_s x_g + iq'_s z_g}. \quad (3.3)$$

At this point, G_0 can be regarded as a superposition of plane waves $e^{ik'_s x + iq'_s z}$ with weights $\frac{e^{-ik'_s x_s}}{2iq'_s}$.

For a plane wave $e^{ik'_s x + iq'_s z}$ incident in an acoustic medium, the reflected wavefield is: (Note that it can be calculated by using the forward scattering series, as in Nita et al. (2004))

$$D(k'_s, q'_s, x_g, z_g = 0) = R(k'_s, q'_s) e^{ik'_s x_g} e^{2iq'_s z_1}. \quad (3.4)$$

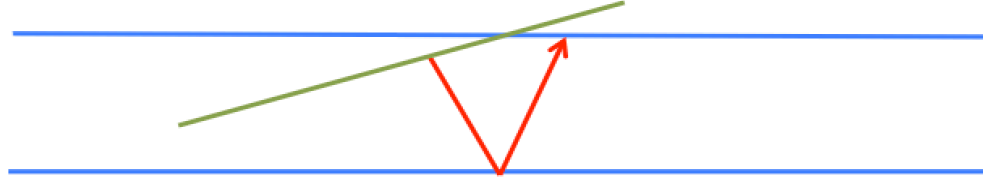


Fig. 3.1: reflection of one plane wave component

Then the total wavefield is (we set $z_g = z_s = 0$):

$$D(x_s, z_s = 0, x_g, z_g = 0, \omega) = \frac{1}{2\pi} \int_{-\omega/c}^{\omega/c} dk'_s \frac{e^{-ik'_s x_s}}{2iq'_s} D(k'_s, q'_s, x_g, z_g = 0). \quad (3.5)$$

Now we get the data at one receiver $(x_g, 0)$ from one delta source $(x_s, 0)$ and rewrite it as:

$$D(x_s, x_g, \omega) = \frac{1}{2\pi} \int_{-\omega/c}^{\omega/c} dk'_s \frac{e^{-ik'_s x_s}}{2iq'_s} R(k'_s, q'_s) e^{ik'_s x_g} e^{2iq'_s z_1} \quad (3.6)$$

This is in the frequency-space domain, whereas the attenuation algorithm works in the frequency-wavenumber domain. After Fourier transforming over the source and receivers, we convert the data to the frequency-wavenumber domain¹.

¹See appendix C for derivation

$$D(k_s, k_g, \omega) = \delta(k_s - k_g) \frac{R(k_s, q_s) e^{2iq_s z_1}}{4\pi i q_s} (-\omega/c < k_s < \omega/c) \quad (3.7)$$

Now we define $b_1(k_s, k_g, \omega)$ as (in the following discussion, we assume that $-\omega/c < k_s < \omega/c$):

$$\begin{aligned} b_1(k_s, k_g, \omega) &= -2iq_s D(k_s, k_g, \omega) \\ &= -\frac{1}{2\pi} \delta(k_s - k_g) R(k_s, q_s) e^{2iq_s z_1}. \end{aligned} \quad (3.8)$$

Then, $b_1(k_s, k_g, \omega)$ and the attenuation algorithm prediction $b_3(k_s, k_g, \omega)$ are related by the 2D internal-multiple attenuation algorithm:

$$\begin{aligned} b_3(k_g, k_s, \omega) &= \int_{-\infty}^{\infty} \int_{-\infty}^{\infty} dk_1 dk_2 \int_{-\infty}^{\infty} dz e^{i(q_g + q_1)z} b_1(k_g, k_1, z) \int_{-\infty}^z dz' e^{i(-q_1 - q_2)z'} b_1(k_1, k_2, z') \\ &\quad \times \int_{z'}^{\infty} dz'' e^{i(q_2 + q_s)z''} b_1(k_2, k_s, z'') \end{aligned}$$

Next with the definition of $b_1(k_s, 2q_s)$ and its prediction $b_3(k_s, 2q_s)$ for 1D pre-stack data, we have:

$$b_1(k_s, k_g, \omega) = -\frac{1}{2\pi} \delta(k_s - k_g) b_1(k_s, 2q_s) \quad (3.9)$$

$$b_3(k_g, k_s, q_g + q_s) = -\frac{1}{(2\pi)^3} \delta(k_g - k_s) b_3(k_s, 2q_s). \quad (3.10)$$

Then, $b_1(k_s, 2q_s)$ and $b_3(k_s, 2q_s)$ are related by the 1D pre-stack algorithm:

$$b_3(k_s, 2q_s) = \int_{-\infty}^{\infty} dz e^{2iq_s z} b_1(k_s, z) \int_{-\infty}^z dz' e^{-2iq_s z'} b_1(k_s, z') \int_{z'}^{\infty} dz'' e^{2iq_s z''} b_1(k_s, z'') \quad (3.11)$$

Ignoring the subscript s, we have

$$b_3(k, 2q) = \int_{-\infty}^{\infty} dz e^{2iqz} b_1(k, z) \int_{-\infty}^z dz' e^{-2iqz'} b_1(k, z') \int_{z'}^{\infty} dz'' e^{2iqz''} b_1(k, z''). \quad (3.12)$$

In the equation, for the first primary, we have

$$b_1(k, 2q) = R(k, q) e^{2iqz_1}, \quad (3.13)$$

and $b_1(k, z)$ is the Fourier transform of $b_1(k, 2q)$ from $2q$ to z .

We can also get the reflection data from the second reflector, and we can obtain a first-order internal multiple as shown in Figure 3.2

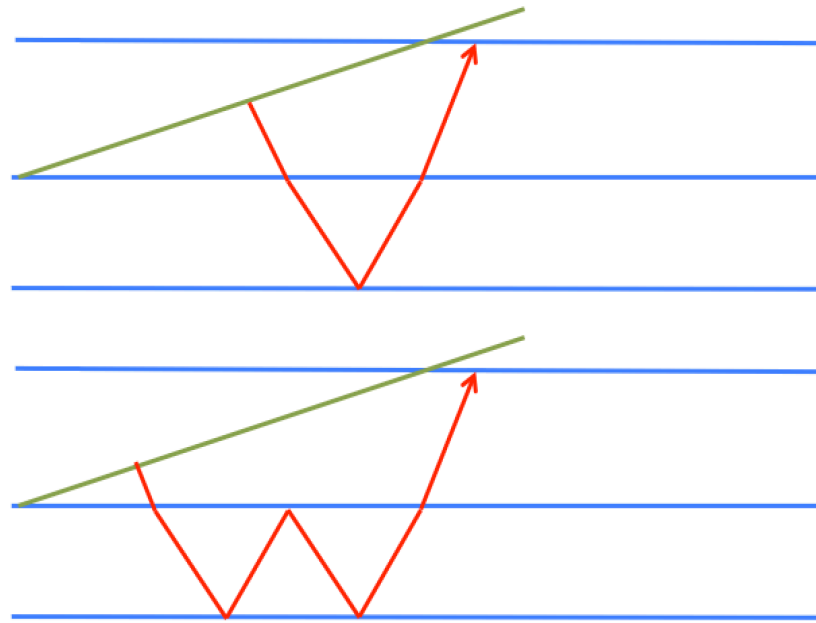


Fig. 3.2: reflection of one plane wave component

Now, b_1 can be written as,

$$\begin{aligned} b_1(k_1, 2q_1) &= R_1(k_1, q_1)e^{2iq_1z_1} \\ &\quad + T_{01}R_2(k_2, q_2)T_{10}e^{2iq_1z_1}e^{2iq_2(z_2-z_1)} \\ &\quad - T_{01}R_2R_1R_2T_{10}e^{2iq_1z_1}e^{4iq_2(z_2-z_1)} \end{aligned} \quad (3.14)$$

Here, q_1 and q_2 are vertical wavenumbers at each layer, and q_2 is a function of q_1 . To Fourier transform from q_1 to z , first we need to substitute q_2 with q_1 .

Using the relation,

$$q_1^2 + k_1^2 = \left(\frac{\omega}{c_1}\right)^2 \quad (3.15)$$

$$q_2^2 + k_2^2 = \left(\frac{\omega}{c_2}\right)^2 \quad (3.16)$$

$$k_1 = k_2, \quad (3.17)$$

we can express q_2 in q_1 and k_1 :

$$\begin{aligned} q_2 &= \sqrt{\left(\frac{c_1^2}{c_2^2} - 1\right)k_1^2 + \frac{c_1^2}{c_2^2}q_1^2} \\ &= \frac{c_1}{c_2}q_1 + \left[\sqrt{\left(\frac{c_1^2}{c_2^2} - 1\right)k_1^2 + \frac{c_1^2}{c_2^2}q_1^2} - \frac{c_1}{c_2}q_1 \right] \\ &= \frac{c_1}{c_2}q_1 + \frac{\left(\frac{c_1^2}{c_2^2} - 1\right)k_1^2}{\sqrt{\left(\frac{c_1^2}{c_2^2} - 1\right)k_1^2 + \frac{c_1^2}{c_2^2}q_1^2 + \frac{c_1}{c_2}q_1}} \\ &= \frac{c_1}{c_2}q_1 + S(k_1, q_1) \end{aligned} \quad (3.18)$$

Now we substitute q_2 with q_1 :

$$\begin{aligned}
 b_1(k_1, 2q_1) &= R_1(k_1, q_1)e^{2iq_1z_1} \\
 &\quad + R'_2(k_1, q_1)e^{2i(z_2-z_1)S(k_1, q_1)}e^{2iq_1(z_1+\frac{c_1}{c_2}(z_2-z_1))} \\
 &\quad - R'_{212}(k_1, q_1)e^{4i(z_2-z_1)S(k_1, q_1)}e^{2iq_1(z_1+\frac{2c_1}{c_2}(z_2-z_1))} \\
 &= R_1(k_1, q_1)e^{2iq_1z_1} \\
 &\quad + R'_2(k_1, q_1)e^{2i(z_2-z_1)S(k_1, q_1)}e^{2iq_1z'_2} \\
 &\quad - R'_{212}(k_1, q_1)e^{4i(z_2-z_1)S(k_1, q_1)}e^{2iq_1(2z'_2-z_1)} \tag{3.19}
 \end{aligned}$$

The predicted internal multiple should be:

$$b_3(k_1, 2q_1) = R'_2(k_1, q_1)R_1(k_1, q_1)R'_2(k_1, q_1)e^{4i(z_2-z_1)S(k_1, q_1)}e^{2iq_1(2z'_2-z_1)} \tag{3.20}$$

Comparing the predicted amplitude of the internal multiple with the actual amplitude of the internal multiple, we have:

$$\begin{aligned}
 R'_{212}(k_1, q_1) &= T_{01}R_2R_1R_2T_{10} \\
 &= \frac{R'_2(k_2, q_2)R_1(k_1, q_1)R'_2(k_2, q_2)}{T_{01}(k_1, q_1)T_{10}(k_1, q_1)} \tag{3.21}
 \end{aligned}$$

We can see that they differed by a factor $T_{01}(k_1, q_1)T_{10}(k_1, q_1)$. That is the attenuation factor for the 1D pre-stack acoustic medium.

3.2 The ISS internal-multiple elimination algorithm for 1D pre-stack data

Now we have the attenuation factor for the 1D pre-stack acoustic medium and it lights the way to extending the 1D normal-incidence algorithm to 1D pre-stack data. Below shows the 1D pre-stack acoustic algorithm. In the 1D pre-stack elimination algorithm, due to the

angle-dependent reflection coefficients, we can no longer just integrate the data in the k-z domain to get the reflection coefficients-we need to go to the k-q domain in which each pair k-q corresponds to a reflection coefficient. The differences between the 1D pre-stack algorithm and the 1D normal incidence algorithm are that the 1D pre-stack algorithm has one more variable k, and it uses the reflection coefficients in the k-q domain instead of the direct integral in the k-z domain.

$$b_E^{IM}(k, 2q) = \int_{-\infty}^{\infty} dz e^{2iqz} b_1(k, z) \int_{-\infty}^{z-\varepsilon_1} dz' e^{-2iqz'} F[b_1(k, z')] \int_{z'+\varepsilon_2}^{\infty} dz'' e^{2iqz''} b_1(k, z'') \quad (3.22)$$

$$\begin{aligned} F[b_1(k, z)] &= \frac{1}{2\pi} \int_{-\infty}^{\infty} \int_{-\infty}^{\infty} dz' dq' \\ &\times \frac{e^{-iq'z} e^{iq'z'} b_1(k, z')} {[1 - \int_{-\infty}^{z'-\varepsilon} dz'' b_1(k, z'') e^{iq'z''} \int_{z''-\varepsilon}^{z''+\varepsilon} dz''' g^*(k, z''') e^{-iq'z''''}]^2 [1 - |\int_{z'-\varepsilon}^{z'+\varepsilon} dz'' g(k, z'') e^{iq'z''}|^2]} \end{aligned} \quad (3.23)$$

$$g(k, z) = \frac{1}{2\pi} \int_{-\infty}^{\infty} \int_{-\infty}^{\infty} dz' dq' \frac{e^{-iq'z} e^{iq'z'} b_1(k, z')}{1 - \int_{-\infty}^{z'-\varepsilon} dz'' b_1(k, z'') e^{iq'z''} \int_{z''-\varepsilon}^{z''+\varepsilon} dz''' g^*(k, z''') e^{-iq'z''''}} \quad (3.24)$$

3.3 A numerical test for 1D pre-stack synthetic elastic PP data

We test the 1D pre-stack internal-multiple elimination algorithm for an four-reflector elastic model shown in figure 3.3. Figure 3.4 shows the PP data generated from this model by reflectivity method. Figure 3.5 and figure 3.6 show a section (2.8s-3.1s) of the data and attenuation and elimination prediction results.

1D pre-stack ISS internal-multiple elimination algorithm

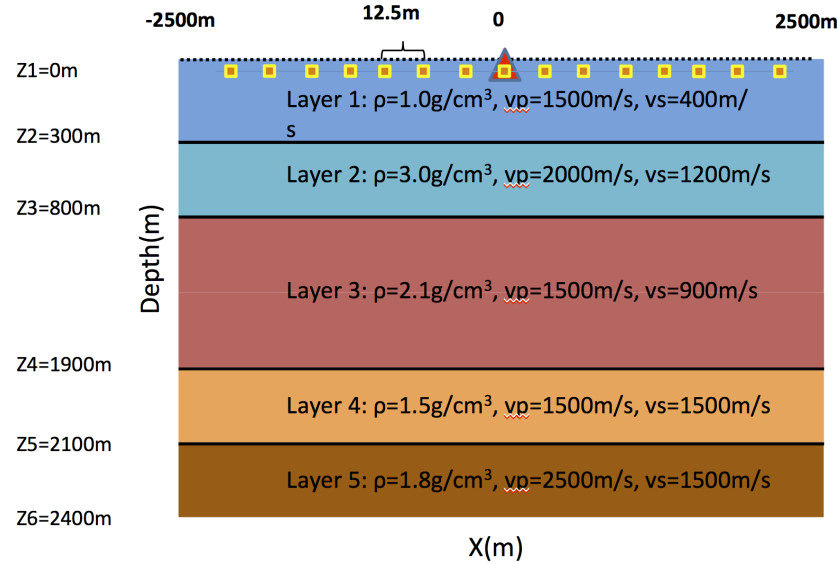


Fig. 3.3: model

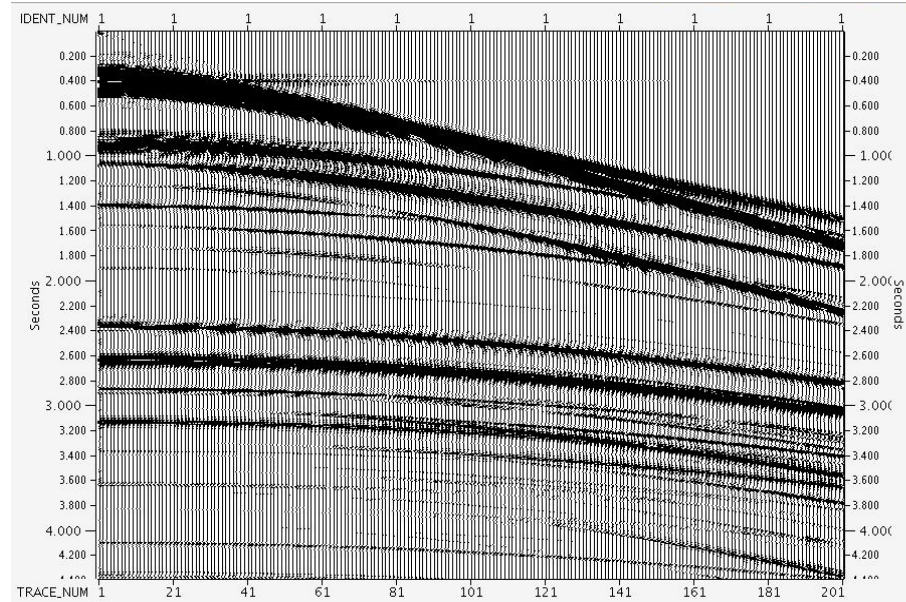


Fig. 3.4: PP data

The left picture in figure 3.5 shows a section in the input data. In this section ,there are 3 major events interfering with each other: a converted P primary, an internal multiple generated from the first reflector and another internal multiple generated from the third

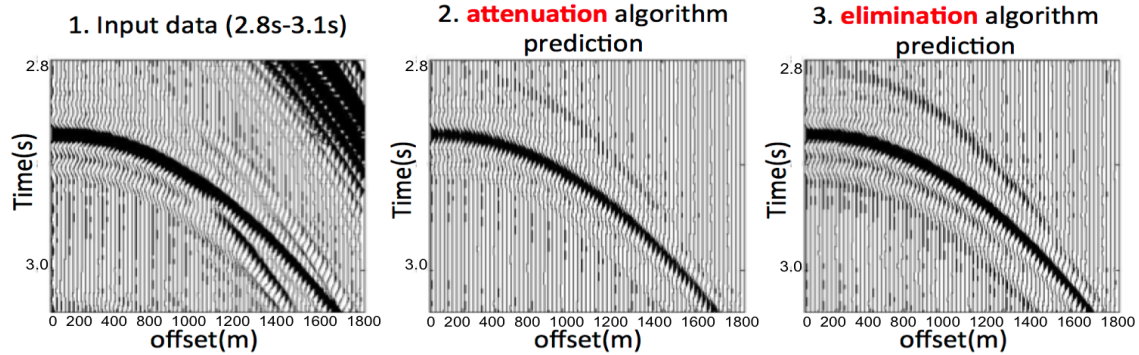


Fig. 3.5: A section of the input data and prediction. Left: input data. Middle: attenuation algorithm prediction. Right:elimination algorithm prediction.

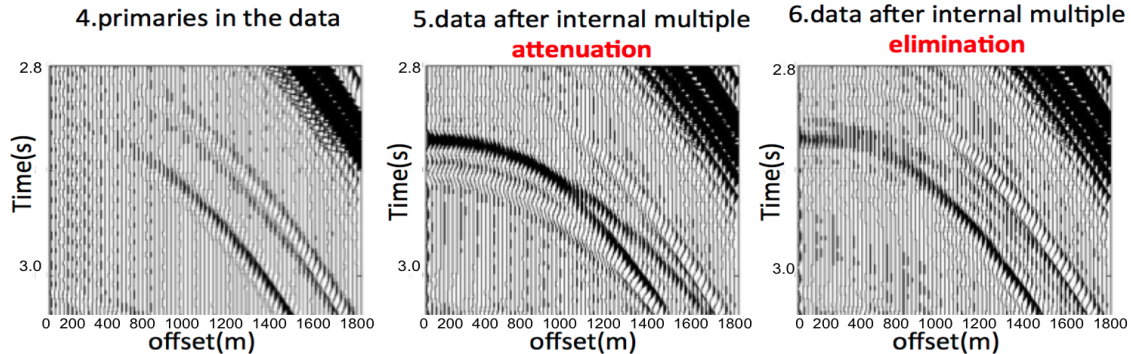


Fig. 3.6: Left: primaries in the input data. Middle: data after internal multiples being attenuated. Right: data after internal multiples being eliminated.

reflector. The middle picture in figure 3.5 shows the attenuation algorithm predicted internal multiples, it clearly shows the predicted internal multiples have correct time and approximate amplitude. The right picture in figure 3.5 shows the elimination algorithm prediction, the time is correct and the amplitude is more accurate. The left picture in figure 3.6 shows the primaries in the data. (Because it is a synthetic test, we can generate only the primaries and use them as a benchmark.) The middle picture in figure 3.6 shows the result by subtracting the attenuation algorithm prediction from the data. The internal multiples has been reduced, but there still remains residues. The right picture in figure 3.6 shows the result by subtracting the elimination algorithm prediction from the data. We can

see that the multiples has been removed and the primary is recovered. (Note that there is some small residual due to: (1) the inaccuracy of the numerical Hankel transform and (2) the assumption of an acoustic relationship between transmission coefficients and reflection coefficients. The Hankel transform is used here because the earth is assumed to be 1D and the data is generated by a 3D source. The input is data recorded by a line of receivers along a radius within a cylindrical coordinate system and that gives rise to the Hankel transform. If we had a full area coverage of receivers, we can use a Fast Fourier Transform instead of numerical Hankel transform and that will remove the residue due to the numerical Hankel transform. The residue due to the acoustic relationship assumption between transmission and reflection coefficients will be addressed in the future when the elimination method is extended to elastic/anelastic media)

3.4 A limitation of this elimination algorithm and an algorithm to address the limitation

There is a limitation of this elimination algorithm, that is, the primaries in the reflection data that enters the algorithm provides that elimination capability, automatically without requiring the primaries to be identified or in any way separated. The other events in the reflection data, that is, the internal multiples, may alter the amplitude and need assist to completely eliminate the internal multiples. That is a limitation of this elimination algorithm. To deal with this limitation, we can first use ISS internal-multiple attenuation algorithm prediction (b_3) to attenuate the internal multiples in the data (b_1) and then put the subtracted result, i.e., $b_1 + b_3$, which contains primaries and attenuated internal multiples, into the ISS internal-multiple elimination algorithm and predict internal multiples with more accurate amplitude. (Note that in the numerical test, this limitation has very small affect on the prediction, thus we do not need to consider addressing this limitation in this test. However, for certain situation, we need to consider this limitation.)

4. MULTI-DIMENSIONAL ACOUSTIC ISS INTERNAL-MULTIPLE ELIMINATION ALGORITHM

4.1 The first Inverse-Scattering-Series internal-multiple elimination method for a multi-dimensional subsurface

The Inverse-Scattering-Series contains an internal-multiple elimination sub-series. Since the internal-multiple attenuation algorithm is capable to predict the correct time and approximate amplitude for all internal multiples, if we can isolate all terms that can predict the same time as the attenuation algorithm by the initial elimination idea (removing the attenuation factor by the reflection data) in the Inverse-Scattering-Series, then adding all these terms together will give us an elimination algorithm. Since the Inverse-Scattering-Series is a multi-D series, the elimination algorithm/terms identified is a multi-D algorithm. Benefiting from the previous work, the internal-multiple elimination sub-series is:

$$\begin{aligned}
 \text{elimination} &= \frac{\text{attenuation}}{AF_i} \\
 &= \text{attenuation} + \text{attenuation} \times R_i'^2 + \text{attenuation} \times R_i'^4 + \dots \\
 &\quad + \text{attenuation} \times (R_1^2 + R_2 R_2' + \dots + R_{i-1} R_{i-1}') + \dots
 \end{aligned} \tag{4.1}$$

Elimination terms in the ISS are identified. Below shows a 2D version of a higher-order

term in the elimination algorithm that corresponds to the term $\text{attenuation} \times R_i'^2$.

$$\begin{aligned}
 b_E(k_s, k_g, q_g + q_s) = & \\
 \int_{-\infty}^{+\infty} \int_{-\infty}^{+\infty} dk_1 dk_2 \int_{-\infty}^{+\infty} dz_1 b_1(k_g, k_1, z_1) e^{i(q_g + q_1)z_1} \\
 \times \int_{-\infty}^{z_1 - \varepsilon} dz_2 F(k_1, k_2, z_2) e^{-i(q_1 + q_2)z_2} \int_{z_2 + \varepsilon}^{+\infty} dz_3 b_1(k_2, k_s, z_3) e^{i(q_2 + q_s)z_3} & (4.2)
 \end{aligned}$$

$$\begin{aligned}
 F(k_1, k_2, z) = & \\
 \int_{-\infty}^{+\infty} d(q_1 + q_2) e^{-i(q_1 + q_2)z} \int_{-\infty}^{+\infty} \int_{-\infty}^{+\infty} dk' dk'' \int_{-\infty}^{+\infty} dz' b_1(k_1, k', z') e^{i(q_1 + q')z'} \\
 \times \int_{z' - \varepsilon}^{z' + \varepsilon} dz'' b_1(k', k'', z'') e^{-i(q' + q'')z''} \int_{z'' - \varepsilon}^{z'' + \varepsilon} dz''' b_1(k'', k_2, z''') e^{i(q'' + q_2)z'''} & (4.3)
 \end{aligned}$$

Below shows another term that corresponds to $\text{attenuation} \times (R_1^2 + R_2 R'_2 + \dots + R_{i-1} R'_{i-1})$;

$$\begin{aligned}
 b_E(k_s, k_g, q_g + q_s) = & \\
 \int_{-\infty}^{+\infty} \int_{-\infty}^{+\infty} dk_1 dk_2 \int_{-\infty}^{+\infty} dz_1 b_1(k_g, k_1, z_1) e^{i(q_g + q_1)z_1} \\
 \times \int_{-\infty}^{z_1 - \varepsilon} dz_2 F(k_1, k_2, z_2) e^{-i(q_1 + q_2)z_2} \int_{z_2 + \varepsilon}^{+\infty} dz_3 b_1(k_2, k_s, z_3) e^{i(q_2 + q_s)z_3} & (4.4)
 \end{aligned}$$

$$\begin{aligned}
 F(k_1, k_2, z) = & \\
 & \int_{-\infty}^{+\infty} d(q_1 + q_2) e^{-i(q_1+q_2)z} \int_{-\infty}^{+\infty} \int_{-\infty}^{+\infty} dk' dk'' \int_{-\infty}^{+\infty} dz' b_1(k_1, k', z') e^{i(q_1+q')z'} \\
 & \times \int_{-\infty}^{z'-\varepsilon} dz'' b_1(k', k'', z'') e^{-i(q'+q'')z''} \int_{z''-\varepsilon}^{z''+\varepsilon} dz''' g(k'', k_2, z''') e^{i(q''+q_2)z'''} \quad (4.5)
 \end{aligned}$$

$$\begin{aligned}
 g(k_1, k_2, z) = & \\
 & \int_{-\infty}^{+\infty} d(q_1 + q_2) e^{-i(q_1+q_2)z} \int_{-\infty}^{+\infty} \int_{-\infty}^{+\infty} dk' dk'' \int_{-\infty}^{+\infty} dz' b_1(k_1, k', z') e^{i(q_1+q')z'} \\
 & \times \int_{-\infty}^{z'-\varepsilon} dz'' b_1(k', k'', z'') e^{-i(q'+q'')z''} \int_{z''-\varepsilon}^{z''+\varepsilon} dz''' g(k'', k_2, z''') e^{i(q''+q_2)z'''} \quad (4.6)
 \end{aligned}$$

Similar to the extension in the previous sections and in Zou and Weglein (2014) , $F(k_1, k_2, z)$ and $g(k_1, k_2, z)$ are two intermediate functions.

Combining all of these kind of higher-order terms provides the elimination algorithm in a 2D earth. The elimination algorithm for a 3D earth is a straightforward extension. The complete subseries is given in Zou et al. (2016).

4.2 2D acoustic synthetic data example

Figure 4.1 shows the 2D model, the data is generated by finite difference method. There is a hat shape structure in the middle of the model. The shape is designed so that its lower boundary is negatively interfering with an internal multiple. In this synthetic data,

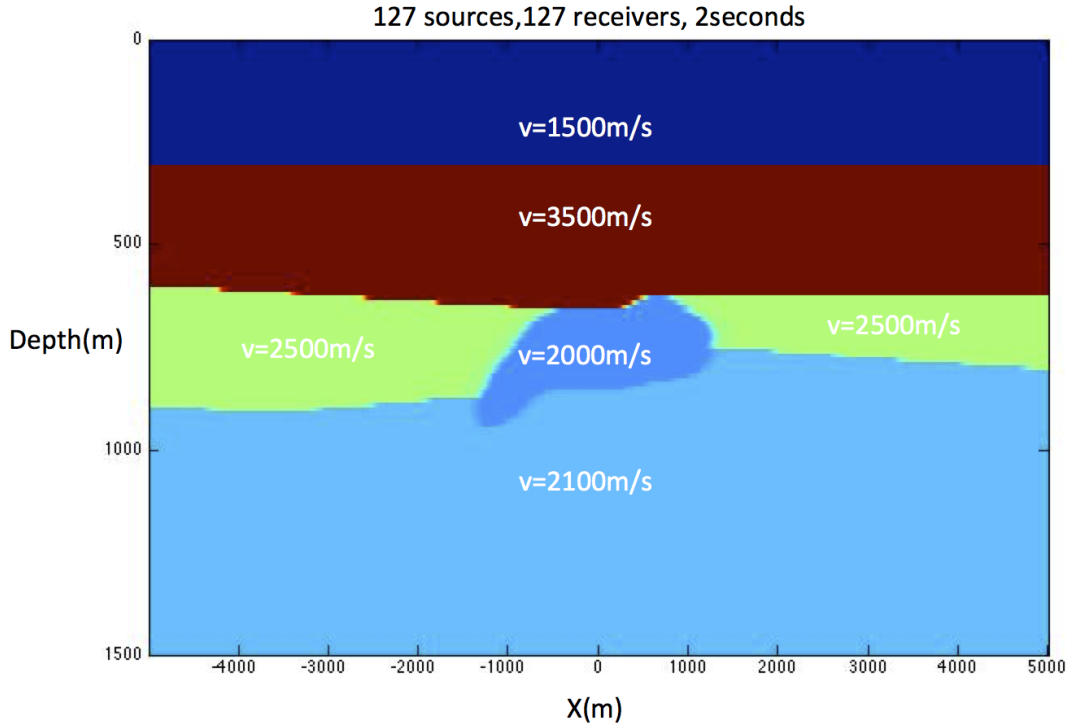


Fig. 4.1: 2D Model

there are 127 shot gathers, each shot gather contains 127 receivers. The source and receiver interval is 30 meters and time interval 0.002s.

Figure 4.2 shows three shot gathers of the input data with source at -450m, 0m, 750m respectively. Figure 4.3 shows three shot gathers of the ISS attenuation algorithm prediction with source at -450m, 0m, 750m respectively. Figure 4.4 shows three shot gathers of the ISS elimination algorithm prediction with source at -450m, 0m, 750m respectively. From these figures we can see the strongest internal multiple is interfere with one primary in the data, especially at small offset.

In order to see the result more clearly, we show the zero offset traces results. Figure 4.5 shows the zero offset traces of the input data. Compared to the model, we can see clearly that the lower boundary of the hat shape is almost invisible because the primary generated by the

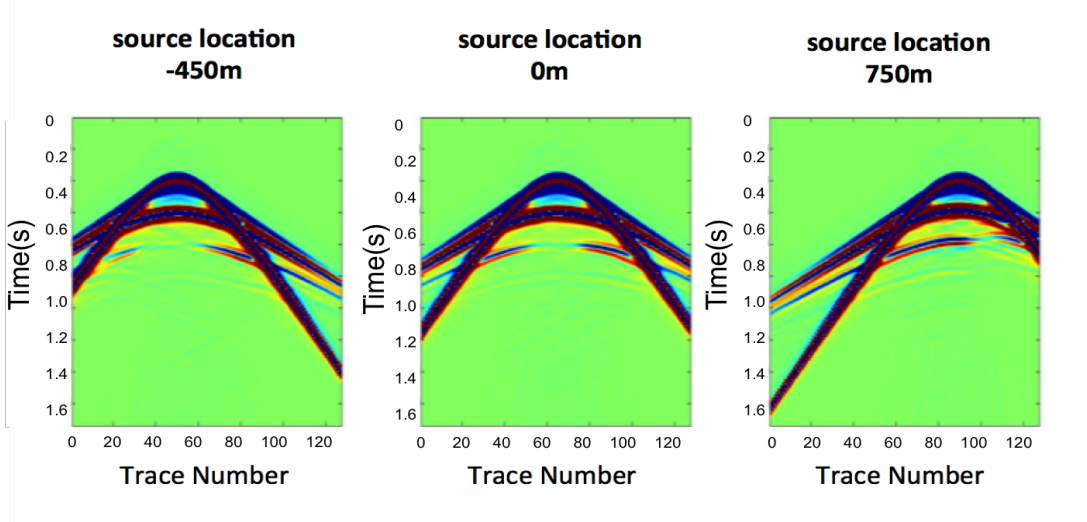


Fig. 4.2: pre-stack data

ISS internal multiple attenuation algorithm prediction

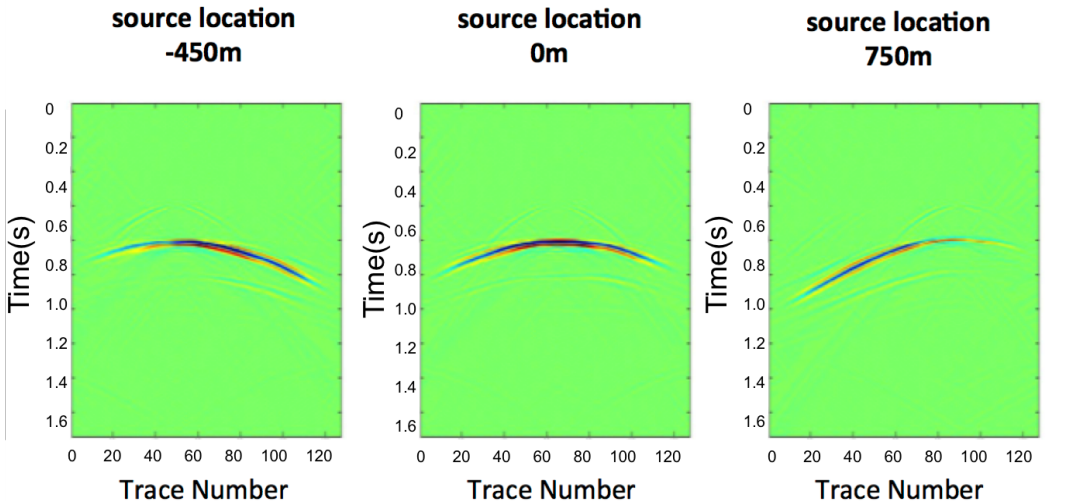


Fig. 4.3: ISS internal-multiple attenuation algorithm prediction

hat's lower boundary is negatively interfere with an internal multiple. Figure 4.6 shows the zero offset traces results after ISS internal-multiple attenuation and adaptive subtraction. We can see the lower boundary of the hat shape is still not visible. It is because the criteria

ISS internal multiple **elimination** algorithm prediction

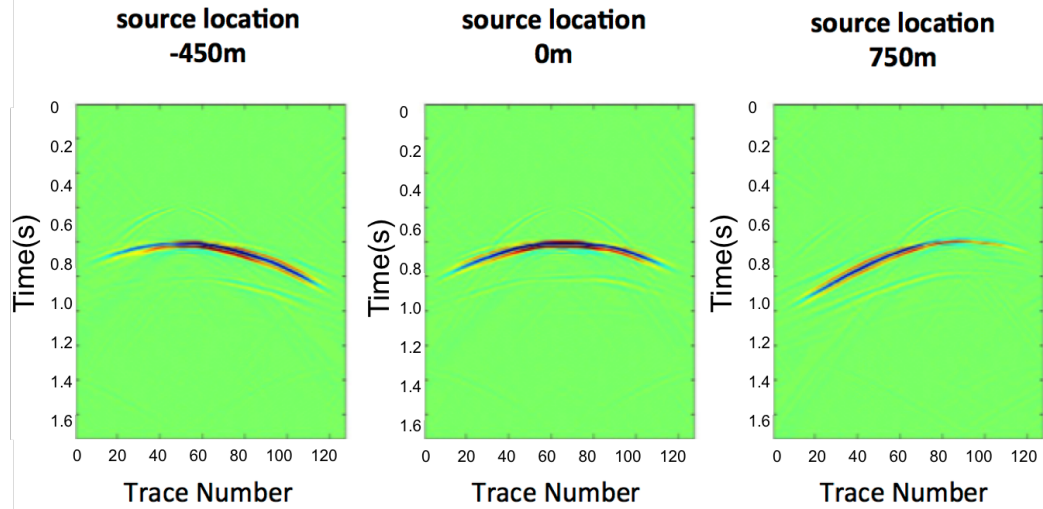


Fig. 4.4: ISS internal-multiple elimination algorithm prediction

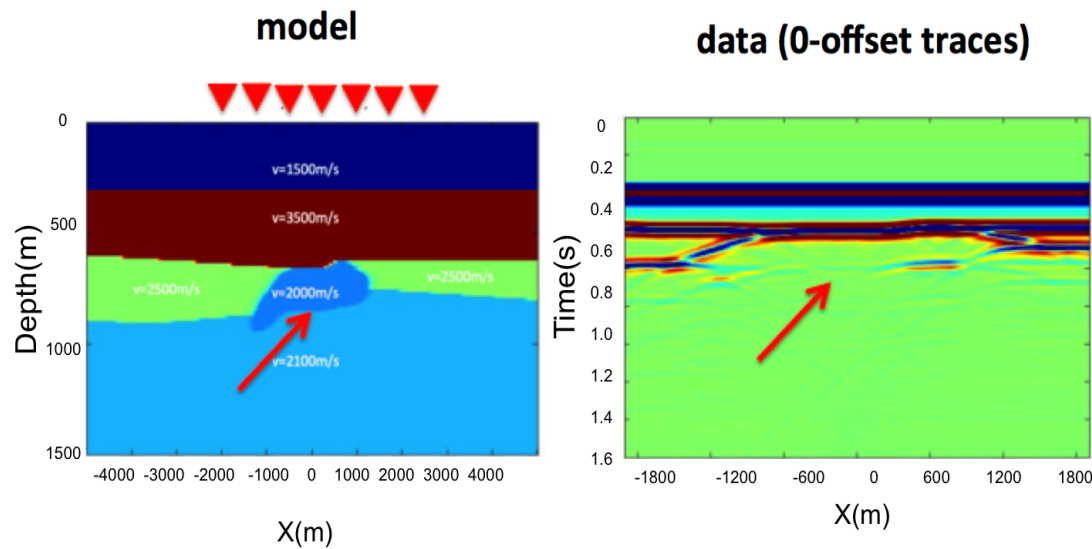


Fig. 4.5: Zero offset traces of data

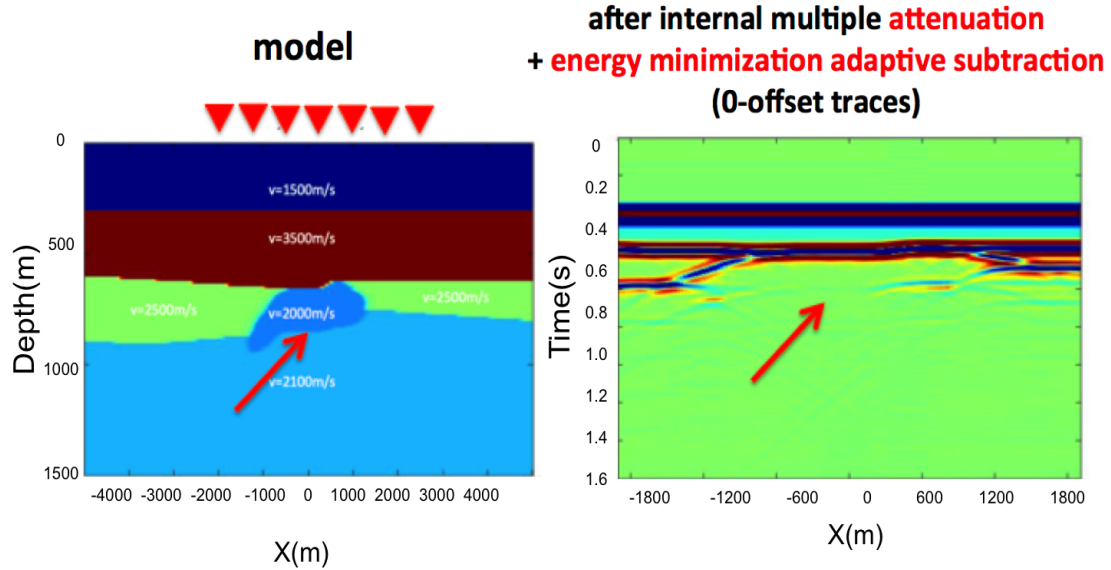


Fig. 4.6: Zero offset traces after ISS internal-multiple attenuation and energy minimization adaptive subtraction

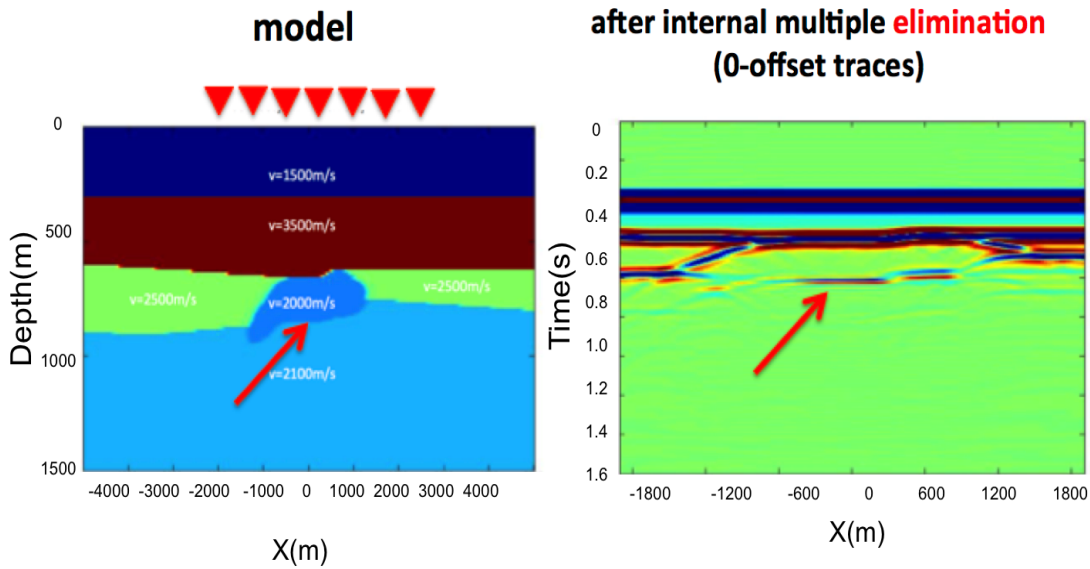


Fig. 4.7: Zero offset traces after ISS internal-multiple elimination

of the energy minimization adaptive subtraction fails, that is, the primary energy after subtraction is larger than the interfering events. Figure 4.7 shows the 0-offset trace results

after internal-multiple elimination. The lower boundary of the hat shape is recovered in the result. It proves that the elimination algorithm can predict both correct time and amplitude and can eliminate internal multiples without touching the primary.

5. A COMPARISON OF THE AMPLITUDE PROPERTIES OF TWO IMPORTANT IMAGING CONDITIONS: 1 THE SPACE-TIME COINCIDENCE OF UP AND DOWN WAVES, AND 2 THE PREDICTED COINCIDENT SOURCE AND RECEIVER EXPERIMENT AT DEPTH AT TIME ZERO

5.1 *Background*

Methods that use the wave equation to perform seismic migration have two ingredients: (1) a wave propagation component and (2) an imaging principle or concept. Claerbout (Claerbout, 1971; Riley and Claerbout, 1976) was the initial and key wave-equation-migration imaging-concept pioneer and algorithm developer, together with Stolt (Stolt (1978)) and Lowenthal (Lowenthal et al. (1985)) and their colleagues, they introduced imaging conditions for locating reflectors at depth from surface-recorded data. The three key imaging conditions that were introduced are:

- I. the exploding-reflector model
- II. time and space coincidence of up and downgoing waves
- III. predicting a source and receiver experiment at a coincident-source-and-receiver subsurface point, and asking for time equals zero (the definition of wave-equation migration)

For a normal-incident spike plane wave on a horizontal reflector, these three imaging concepts are totally equivalent. However, a key point to make clear is that for a non-zero-offset surface seismic-data experiment, with either a one-dimensional or a multi-dimensional sub-

surface, they are no longer equivalent. Wave-equation migration is defined as using the Claerbout Imaging Condition III, predicting a source and receiver experiment at depth at time equals zero. Stolt and his colleagues (Clayton and Stolt, 1981; Stolt and Weglein, 1985; Stolt and Benson, 1986; Stolt and Weglein, 2012; Weglein and Stolt, 1999) extended and formulated the experiment-at-depth concept to allow a separated source and receiver experiment at time equals zero for one way propagating waves. Weglein, Fang and their colleagues (Weglein et al., 2011a;b; Liu, 2013) extended Claerbout III for two way propagating waves.

Claerbout III and Claerbout II have the same principle for both one-way and two-way waves. In order to understand the benefits that the two way wave propagation form of Claerbout III will bring to seismic exploration, we first examine the differences between Claerbout III and other imaging conditions for one way wave. In this paper, we first compare the imaging results of Clearbout III - Stolt migration and its asymptotic form - Kirchhoff migration. Stolt migration is Claerbout III for one-way waves. Kirchhoff migration is its natural approximation. Kirchhoff migration shares some kind of behavior with RTM (Claerbout II), including producing candidate and depending on the coherent summing over candidate. Then we compare the imaging results of Clearbout III - Stolt migration and Clearbout II - RTM. These comparisons and results show that Claerbout III is superior to Claerbout I and II in that it provides the most quantitative and interpretable image amplitude. Claerbout Imaging Condition III predicts a physical experiment with both source and receiver at depth, allowing it to provide the imaging definitiveness and physical interpretation that other imaging conditions cannot match. Claerbout III is also extendable/generalizable to provide an angle dependent reflection coefficient. For the purpose of determining quantitative information on the physical meaning of the image, the clear choice is Claerbout Imaging Condition III.

5.2 Stolt migration (*Clearbout Imaging Condition III* for one way wave) and
Kirchhoff migration (a asymptotic form of Stolt migration)

In this section we give a review of the 2D pre-stack Stolt migration and following Stolt and Weglein (2012) derive an approximate asymptotic 2D Kirchhoff migration algorithm. The 3D expressions are straight forward extensions.

5.2.1 2D Stolt migration

First, we can denote the wavefield as $P(x_g, z_g, x_s, z_s, t)$ for an experiment where a source locates at (x_s, z_s) and an observation point/receiver locates at (x_g, z_g) .

Given a 2D data $D(x_g, x_s, t)$ ¹ with source location $(x_s, z_s = 0)$, receiver location $(x_g, z_g = 0)$, and time t , we have

$$P(x_g, 0, x_s, 0, t) = D(x_g, x_s, t). \quad (5.1)$$

One can perform a Fourier transform over all coordinates:

$$\begin{aligned} P(k_{gx}, 0, k_{sx}, 0, \omega) &= D(k_{gx}, k_{sx}, \omega) \\ &= \int dx_g \int dx_s \int dt D(x_g, x_s, t) e^{i(k_{sx}x_s - k_{gx}x_g + \omega t)} \end{aligned} \quad (5.2)$$

One can predict the data of an experiment where the source depth is z and receiver depth is 0,

$$P(k_{gx}, 0, k_{sx}, z, \omega) = D(k_{gx}, k_{sx}, \omega) e^{-ik_{sz}z}, \quad (5.3)$$

¹In this paper, if sources and receivers are at $z = 0$, we use D to denote the data , otherwise we use P to denote the data/wavefield.

where the vertical wavenumber component k_{sz} is defined as

$$k_{sz} = \frac{\omega}{c} \sqrt{1 - \frac{k_{sx}^2 c^2}{\omega^2}}. \quad (5.4)$$

Similarly, one can predict the data of an experiment where the source depth is z and receiver depth is z ,

$$\begin{aligned} P(k_{gx}, z, k_{sx}, z, \omega) &= P(k_{gx}, 0, k_{sx}, z, \omega) e^{ik_{gz}z} \\ &= D(k_{gx}, k_{sx}, \omega) e^{i(k_{gz} - k_{sz})z}, \end{aligned} \quad (5.5)$$

where the vertical wavenumber component k_{gz} is

$$k_{gz} = -\frac{\omega}{c} \sqrt{1 - \frac{k_{gx}^2 c^2}{\omega^2}}. \quad (5.6)$$

If we make two inverse Fourier transform of k_{gx} and k_{sx} to the same x , we can predict the data of an experiment where a source and a receiver are both at location (x, z) ,

$$\begin{aligned} P(x, z, x, z, \omega) &= \frac{1}{(2\pi)^2} \int dk_{sx} e^{-ik_{sx}x} \int dk_{gx} e^{ik_{gx}x} P(k_{gx}, z, k_{sx}, z, \omega) \\ &= \frac{1}{(2\pi)^2} \int dk_{sx} e^{-i(k_{sz}z + k_{sx}x)} \int dk_{gx} e^{i(k_{gz}z + k_{gx}x)} D(k_{gx}, k_{sx}, \omega) \end{aligned} \quad (5.7)$$

Next, letting the time of the wavefield to be zero, one can get the 2D Stolt migration image,

$$\begin{aligned} M^{Stolt}(x, z) &= \frac{1}{2\pi} \int d\omega e^{-i\omega t} P(x, z, x, z, \omega)|_{t=0} \\ &= \frac{1}{(2\pi)^3} \int d\omega \int dk_{sx} e^{-i(k_{sz}z + k_{sx}x)} \int dk_{gx} e^{i(k_{gz}z + k_{gx}x)} D(k_{gx}, k_{sx}, \omega) \end{aligned} \quad (5.8)$$

where $M^{Stolt}(x, z)$ is the image function ².

²In Stolt and Weglein (2012), the image function $M^{Stolt}(x, z)$ has a half-integral filter. In this section we do not include the half-integral filter.

5.2.2 2D Kirchhoff migration

Following Stolt and Weglein (2012), one can derive the Kirchhoff migration from Stolt migration.

First, rewriting the 2D Stolt migration algorithm ,i.e., equation 5.8 with the data in space-time domain, one can obtain

$$M^{Stolt}(x, z) = \frac{1}{(2\pi)^3} \int \int \int d\omega dx_g dx_s \int dk_{sx} e^{-i(k_{sz}z + k_{sx}(x - x_s))} \int dk_{gx} e^{i(k_{gz}z + k_{gx}(x - x_g))} \\ \int dt e^{i\omega t} D(x_g, x_s, t) \quad (5.9)$$

An asymptotic approximation can be made with the stationary phase approximation,

$$\int dk_{sx} e^{-i(k_{sz}z + k_{sx}(x - x_s))} \simeq e^{-i\omega r_s/c} \sqrt{\frac{2\pi i\omega z^2}{cr_s^3}} \quad (5.10)$$

$$\int dk_{gx} e^{i(k_{gz}z + k_{gx}(x - x_g))} \simeq e^{-i\omega r_g/c} \sqrt{\frac{2\pi i\omega z^2}{cr_g^3}} \quad (5.11)$$

$$r_s = \sqrt{z^2 + (x - x_s)^2} \quad (5.12)$$

$$r_g = \sqrt{z^2 + (x - x_g)^2} \quad (5.13)$$

$$r = r_s + r_g \quad (5.14)$$

One can obtain the approximate asymptotic 2D Kirchhoff migration,

$$\begin{aligned}
M^{Kirchhoff}(x, z) &= \frac{z^2}{(2\pi)^2 c} \int dx_g \int dx_s \int dt \frac{D(x_g, x_s, t)}{(r_s r_g)^{3/2}} \int d\omega i\omega e^{i\omega(t-r/c)} \\
&= \frac{z^2}{(2\pi)^2 c} \int dx_g \int dx_s \int d\omega i\omega e^{-i\omega r/c} \frac{D(x_g, x_s, \omega)}{(r_s r_g)^{3/2}} \\
&= \frac{z^2}{(2\pi)^2 c} \int dx_g \int dx_s \int d\omega i\omega \int dt e^{-i\omega t} \delta(t - r/c) \frac{D(x_g, x_s, \omega)}{(r_s r_g)^{3/2}} \\
&= \frac{z^2}{(2\pi)^2 c} \int dx_g \int dx_s \int dt \delta(t - r/c) \int d\omega i\omega e^{-i\omega t} \frac{D(x_g, x_s, \omega)}{(r_s r_g)^{3/2}} \\
&= -\frac{z^2}{2\pi c} \int dx_g \int dx_s \int dt \delta(t - r/c) \frac{\frac{d}{dt} D(x_g, x_s, t)}{(r_s r_g)^{3/2}} \\
&= -\frac{z^2}{2\pi c} \int dx_g \int dx_s \frac{\frac{d}{dt} D(x_g, x_s, t)|_{t=r/c}}{(r_s r_g)^{3/2}}
\end{aligned} \tag{5.15}$$

In the last 4 steps use the following Fourier transform convention,

$$D(x_g, x_s, \omega) = \int dt D(x_g, x_s, t) e^{i\omega t} \tag{5.16}$$

$$D(x_g, x_s, t) = \frac{1}{2\pi} \int d\omega D(x_g, x_s, \omega) e^{-i\omega t} \tag{5.17}$$

and

$$\int d\omega i\omega D(x_g, x_s, \omega) e^{-i\omega t} = -2\pi \frac{d}{dt} D(x_g, x_s, t). \tag{5.18}$$

Equation 5.15 is the 2D Kirchhoff migration formula. It is a weighted summation of the data along a trajectory of travel-times corresponding to ray-paths from the source to image point and then to receiver.

5.3 Analysis and numerical tests for the differences of Stolt migration and Kirchhoff migration due to the stationary phase approximation

As we have discussed in the previous section, the differences of Stolt migration and Kirchhoff migration are due to two stationary phase approximations, i.e., equation 5.10 and 5.11. In this section, we analyze and test the effect due to receiver side stationary phase approximation, while the source side effect is similar.

5.3.1 Receiver side stationary phase approximation

Following section 2, given a 2D data $P(x_g, z_g, x_s, z_s, \omega)$ with (x_s, z_s) the sources location, (x_g, z_g) the receivers location and ω the frequency, we can predict the wavefield $P(x, z, x_s, z_s, \omega)$ at (x, z) by Stolt migration algorithm,

$$P^{Stolt}(x, z, x_s, z_s, \omega) = \frac{1}{2\pi} \int dx_g \int dk_{gx} e^{i(k_{gz}(z-z_g)+k_{gx}(x-x_g))} P(x_g, z_g, x_s, z_s, \omega) \quad (5.19)$$

Apply the stationary phase approximation

$$\int dk_{gx} e^{i(k_{gz}(z-z_g)+k_{gx}(x-x_g))} \simeq e^{-i\omega r_g/c} \sqrt{\frac{2\pi i\omega(z-z_g)^2}{cr_g^3}},$$

of the receiver side, we have

$$P^{Asymptotic}(x, z, x_s, z_s, \omega) = \frac{1}{2\pi} \int dx_g e^{-i\omega r_g/c} \sqrt{\frac{2\pi i\omega(z-z_g)^2}{cr_g^3}} P(x_g, z_g, x_s, z_s, \omega) \quad (5.20)$$

$P^{Asymptotic}(x, z, x_s, z_s, \omega)$ is the predicted wavefield at (x, z) generated by a source at (x_s, z_s) using the Kirchhoff-like asymptotic algorithm.

5.3.2 Numerical tests

In this test, we use the Cagniard-de Hoop method (Appendix D) to generate the synthetic data for an acoustic one reflector model shown in figure 5.1. The Reflector depth z_d is 2,000m; source location is $(x_s = 0m, z_s = 0m)$; receiver depth is $z_g = 400m$; receiver interval dx is 4m; time sampling interval dt is 0.001s ($T_{max} = 5s$). Velocities are 2,000m/s and 1,000m/s in the first and second medium, respectively. The generated synthetic data is shown in figure 5.3.

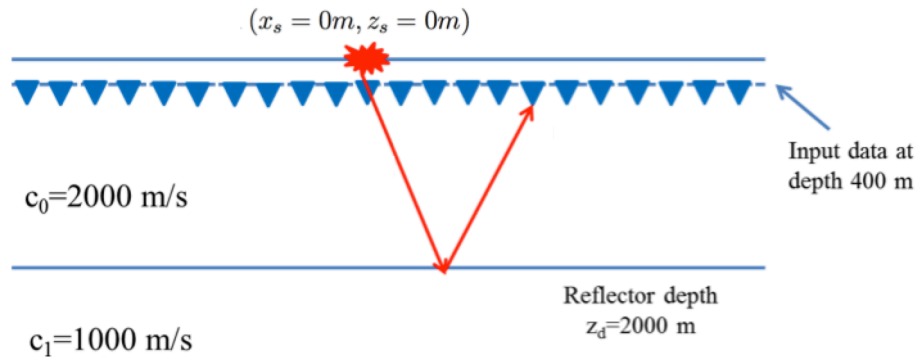


Fig. 5.1: Model to generate CdH synthetic test data as input.

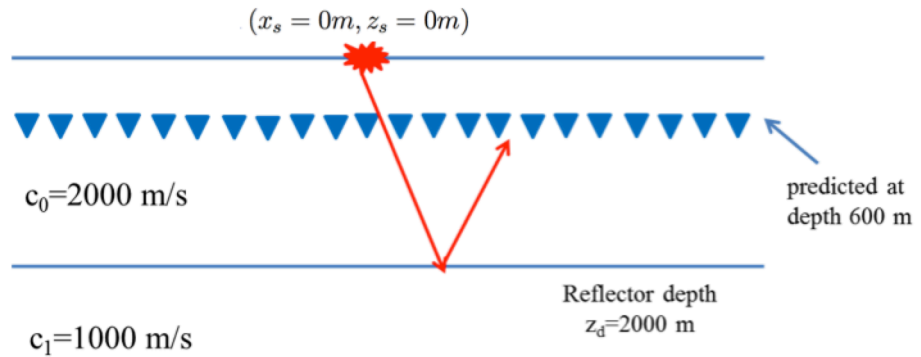


Fig. 5.2: Predicted wavefield at depth 600 m.

Given the data $P(x_g, z_g, x_s, z_s, \omega)$ with source location $(x_s = 0m, z_s = 0m)$ and receiver

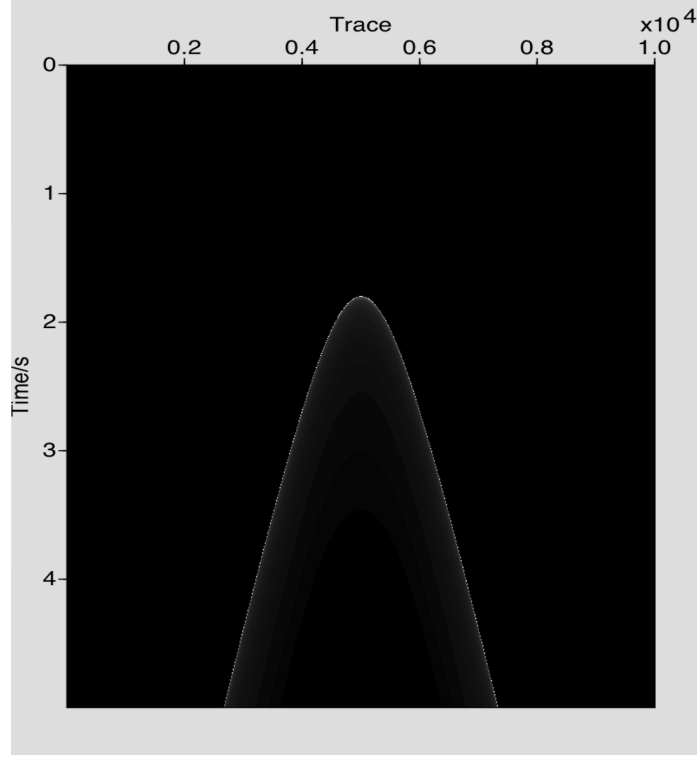


Fig. 5.3: CdH synthetic test data generated from the one reflector model.

depth $z_g = 400m$, we compare the predicted wavefield $P^{Stolt}(x, z, x_s, z_s, \omega)$ and $P^{Asymptotic}(x, z, x_s, z_s, \omega)$ with the exact wavefield P^{CdH} at depth $z=600m$ (at 0m offset and 2,000m offset). In all these following figures, the black line is the exact data generated by using the Cagniard-de Hoop method at depth $z = 600m$, the red line is the asymptotic prediction result $P^{Asymptotic}$, and the blue line is the wave-equation prediction result P^{Stolt} , respectively.

The Stolt migration algorithm prediction of the receivers at depth takes a highly nonlinear dependence of the phase in equation 5.19 (from k_{gz}) and the Kirchhoff-like asymptotic approximation replace it with a liner dependence on the phase in equation 5.20. The resultant difference in spectrum at the low end has a dramatic impact on subsequent imaging steps, and makes the Kirchhoff-like asymptotic migration method not an approximated source and receiver coincident at time equals zero.

A Comparison of the amplitude properties of two important imaging conditions

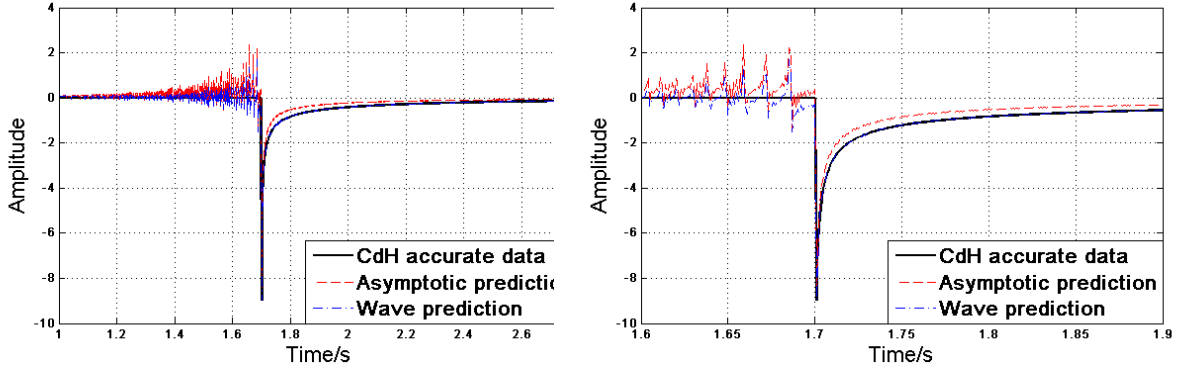


Fig. 5.4: Left: Space-time domain comparison at $x=0m$, $z=600m$, 1.0s to 2.8s. Right: Zoom-in of Left figure from 1.6s to 1.9s. (The amplitude does not have units.)

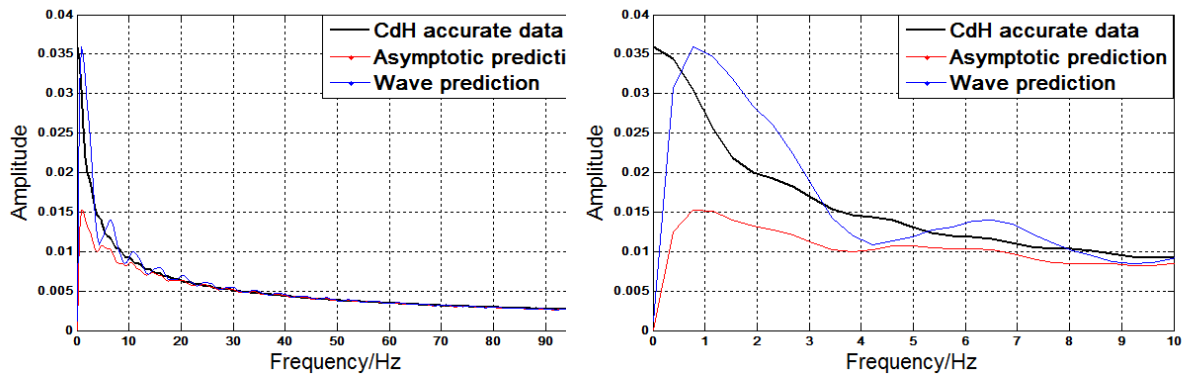


Fig. 5.5: Left: Space-frequency domain comparison at $x=0m$, $z=600m$, 0Hz-100Hz. Right: Zoom-in of left figure from 0Hz to 10Hz. (The amplitude does not have units.)

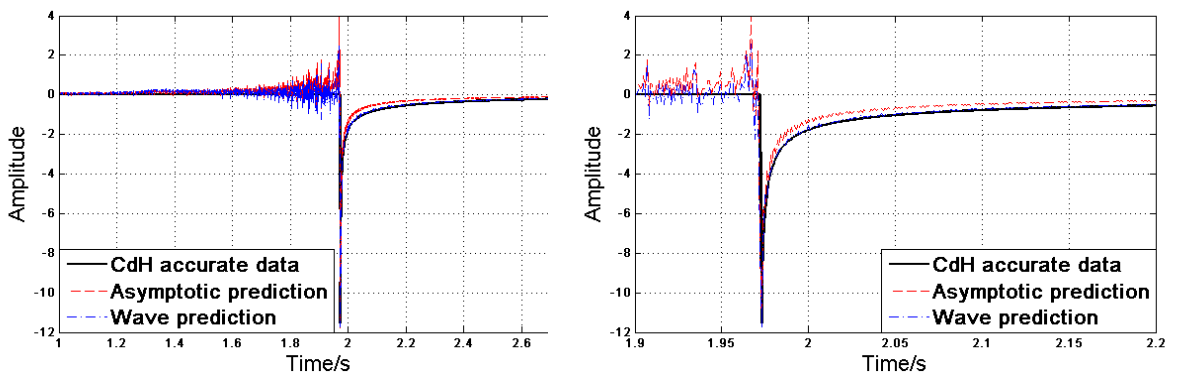


Fig. 5.6: Left: Space-time comparison at $x=2,000m$, $z=600m$, 1.0s to 2.8s. Right: Zoom-in of left figure from 1.9s to 2.2s. (The amplitude does not have units.)

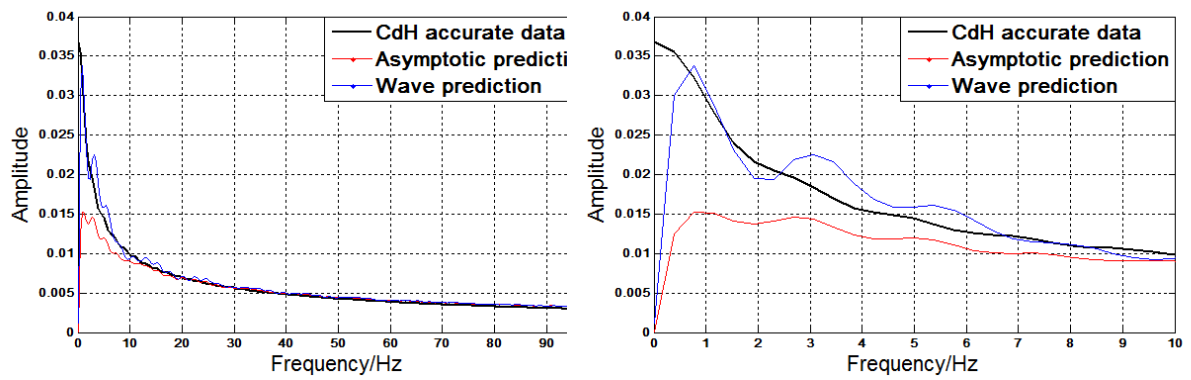


Fig. 5.7: Left: Space-frequency domain comparison at $x=2,000m$, $z=600m$, 0Hz-100Hz. Right: Zoom-in of left figure from 0Hz to 10Hz. (The amplitude does not have units.)

5.4 Obtaining the angle dependent reflection coefficient from Stolt migration and
Kirchhoff migration

5.4.1 Obtaining the angle dependent reflection coefficient from Stolt migration

Wave-equation migration, i.e., migration algorithms such as Stolt migration utilizing Claerbout Imaging Condition III, can be extended to predict non-zero offset data at depth and provide imaging result with subsurface angle information. In order to obtain the subsurface angle information, we first change the integral variables in the wave equation migration formula from k_{sx}, k_{gx}, ω to k_x, k_h, k_z , where

$$\begin{aligned} k_z &\equiv k_{gz} - k_{sz} \\ &= -\frac{\omega}{c} \left(\sqrt{1 - \frac{k_{gx}^2 c^2}{\omega^2}} + \sqrt{1 - \frac{k_{sx}^2 c^2}{\omega^2}} \right) \end{aligned} \quad (5.21)$$

$$k_x \equiv k_{gx} - k_{sx} \quad (5.22)$$

$$k_h \equiv k_{gx} + k_{sx} \quad (5.23)$$

the Jacobian for a change of variables is

$$|\text{Det} \left[\frac{\partial(k_x, k_h, k_z)}{\partial(k_{sx}, k_{gx}, \omega)} \right]| = \frac{2\omega k_z}{c^2 k_{sx} k_{gx}}, \quad (5.24)$$

and the Stolt migration formula equation 5.8 can be rewritten as

$$M^{Stolt}(x, z) = \frac{c^2}{2(2\pi)^3} \int dk_z \int dk_x \int dk_h D(k_{gx}, k_{sx}, \omega) \frac{k_{sz} k_{gz}}{\omega k_z} e^{ik_z z} e^{ik_x x}. \quad (5.25)$$

In equation 5.25, since two of the integrals are inverse Fourier transform, we can obtain the image result in k_x , k_z domain

$$M^{Stolt}(k_x, k_z) = \frac{c^2}{4\pi^2} \int dk_h D(k_{gx}, k_{sx}, \omega) \frac{k_{sz}k_{gz}}{\omega k_z}. \quad (5.26)$$

Now the formula only contains an integral of k_h , which is the Fourier conjugate of subsurface offset x_h . We obtain the migration imaging result with subsurface offset information,

$$M^{Stolt}(k_x, k_z, k_h) = \frac{c^2}{4\pi^2} \frac{k_{sz}k_{gz}}{\omega k_z} D(k_{gx}, k_{sx}, \omega). \quad (5.27)$$

From equation 5.27, we can easily get angle dependent reflection coefficient as well as other angle dependent information.

5.4.2 Obtaining the angle dependent reflection coefficient from kirchhoff migration

Obtaining the angle dependent reflection coefficient by interpreting the Kirchhoff migration result as a fictitious experiment

In equation 5.15, $M^{Kirchhoff}(x, z)$ is Kirchhoff migration image. Although it is a function of x and z , $M^{Kirchhoff}(x, z)$ is not directly related to the reflection coefficient at image point (x, z) . It has limited value (if any) in being interpreted as a reflection coefficient, let alone as the angle dependence of a reflection coefficient. A coincident source and receiver experiment, directly above a reflector at small positive time, is related to the reflection coefficient of that local reflection point. If the migration concept does not correspond to that experiment at depth, one could be able to correctly locate structure but cannot obtain the exact local reflection coefficient. If you nevertheless decide to interpret $M^{Kirchhoff}(x, z)$ in equation 5.15 as though it was the output of an imagined or fictitious zero offset experiment at $t = 0$,

then taking that leap we would write

$$M^{Kirchhoff}(x, z) = M^{Kirchhoff}(x, z, x_h = 0). \quad (5.28)$$

Furthermore, and in addition for the interpretation of the right hand member of equation 5.28 we will assume by causality that for $x_h \neq 0$ at $t = 0$ the measurement would be zero, that is

$$M^{Kirchhoff}(x, z, x_h) = 0 \quad \text{for } x_h \neq 0. \quad (5.29)$$

By assuming this interpretation to Kirchhoff migration, we bent over backwards to allow a way to compare $M^{Stolt}(x, z, x_h)$ with $M^{Kirchhoff}(x, z, x_h)$ in terms of amplitude information from the actual and fictitious experiment output by Stolt migration and Kirchhoff migration, respectively.

Obtaining the angle dependent reflection coefficient by an alternative ray-theory-based algorithm

According to equation 5.15

$$M^{Kirchhoff}(x, z) = -\frac{z^2}{2\pi c} \int dx_g \int dx_s \frac{\frac{d}{dt} D(x_g, x_s, t)|_{t=r/c}}{(r_s r_g)^{3/2}},$$

Kirchhoff migration is a weighted summation of the derivative of data with respect to time over all sources and receiver positions, along a travel-time trajectory (shown in figure 5.8) from the source to the image point and then to the receiver.

As pointed out in Stolt and Weglein (2012), the formula 5.15 does not imply that the summation must be over all sources and receivers. One can pluck out a subset of the complete data set, corresponding to a line or curve on the surface, and consider that as a

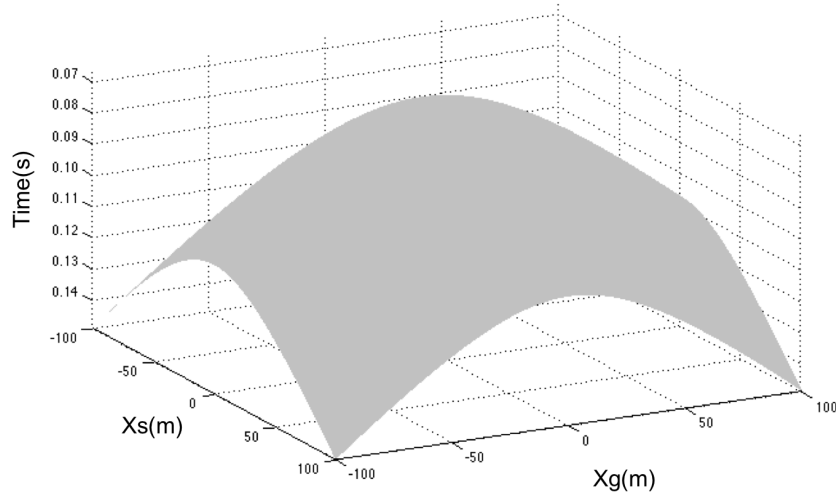


Fig. 5.8: an example of trajectory function $t(x_s, x_g) = r/c$

partial migration, that related to what portion of the data contributes to the migration result (given by 5.15).

Here we are going to show a ray-theory-based algorithm to choose a specific subset of the complete data set, corresponding to a constant incident/dip angle. In Kirchhoff migration, for every image point, we can calculate an incident angle and a dip angle for each source and receiver, as shown in figure 5.9.

First we can calculate two new variables ξ and η ;

$$\xi = \tan\gamma = \frac{-(x_s - x)\sqrt{(x - x_g)^2 + z^2} + (x_g - x)\sqrt{(x - x_s)^2 + z^2}}{z(\sqrt{(x - x_g)^2 + z^2} + \sqrt{(x - x_s)^2 + z^2})} = \frac{-(x_s - x)r_g + (x_g - x)r_s}{zr} \quad (5.30)$$

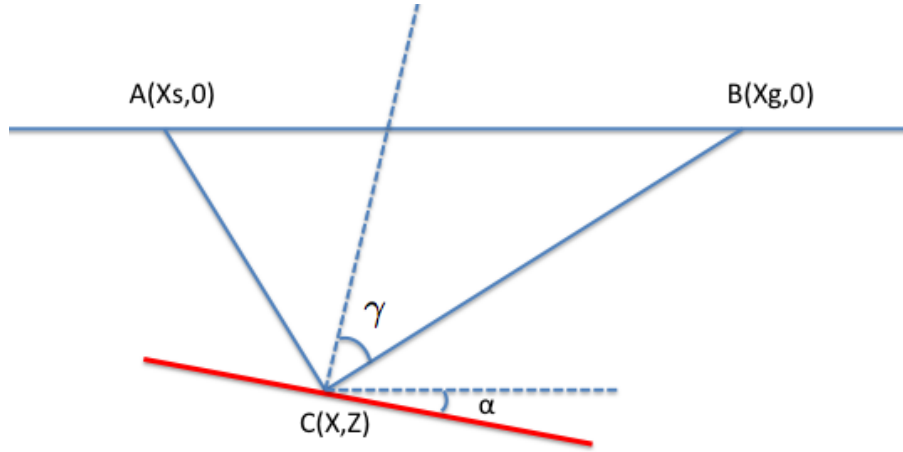


Fig. 5.9: For every image point $C(x, z)$ we can calculate an incident angle γ and a dip angle α for each source $A(x_s, 0)$ and receiver $B(x_g, 0)$.

$$\eta = \tan \alpha = \frac{(x_s - x)\sqrt{(x - x_g)^2 + z^2} + (x_g - x)\sqrt{(x - x_s)^2 + z^2}}{z(\sqrt{(x - x_g)^2 + z^2} + \sqrt{(x - x_s)^2 + z^2})} = \frac{(x_s - x)r_g + (x_g - x)r_s}{zr}, \quad (5.31)$$

where γ is the incident angle and α is the dip angle. The angle convention is defined as follows:

$$\begin{aligned} &\text{when } x_g \geq x_s \quad \gamma \in [0, \frac{\pi}{2}) \\ &\text{when } x_g < x_s \quad \gamma \in (-\frac{\pi}{2}, 0) \\ &\text{when } (x_g - x) \geq (x - x_s) \quad \alpha \in [0, \frac{\pi}{2}) \\ &\text{when } (x_g - x) < (x - x_s) \quad \alpha \in (-\frac{\pi}{2}, 0) \end{aligned}$$

Now we can rearrange the 2D Kirchhoff migration from integrals of source and receiver

locations to integrals of ξ and η :

$$\begin{aligned} M^{Kirchhoff}(x, z) &= -\frac{z^2}{2\pi c} \int dx_g \int dx_s \frac{\frac{d}{dt}D(x_g, x_s, t)|_{t=r/c}}{(r_s r_g)^{3/2}} \\ &= -\frac{z^2}{2\pi c} \int d\xi \int d\eta \left| \frac{\partial(x_s, x_g)}{\partial(\xi, \eta)} \right| \frac{\frac{d}{dt}D(x_g, x_s, t)|_{t=r/c}}{(r_s r_g)^{3/2}} \end{aligned} \quad (5.32)$$

Then we have

$$\begin{aligned} M^{Kirchhoff}(x, z, \xi, \eta) &= -\frac{z^2}{2\pi c} \left| \frac{\partial(x_s, x_g)}{\partial(\xi, \eta)} \right| \frac{\frac{d}{dt}D(x_g, x_s, t)|_{t=r/c}}{(r_s r_g)^{3/2}} \\ &= \frac{z^2 r^2}{4\pi c (r_s r_g)^{3/2}} \frac{d}{dt}D(x_g, x_s, t)|_{t=r/c}, \end{aligned} \quad (5.33)$$

where the Jacobian $\left| \frac{\partial(x_s, x_g)}{\partial(\xi, \eta)} \right|$ can be calculated as follows:

$$\frac{\partial \xi}{\partial x_s} = \frac{(x - x_g)(x - x_s)r_g - z^2 r_g - r_s r_g^2}{z r_s r^2} \quad (5.34)$$

$$\frac{\partial \xi}{\partial x_g} = \frac{-(x - x_g)(x - x_s)r_s + z^2 r_s + r_s^2 r_g}{z r_g r^2} \quad (5.35)$$

$$\frac{\partial \eta}{\partial x_s} = \frac{(x - x_g)(x - x_s)r_g + z^2 r_g + r_s r_g^2}{z r_s r^2} \quad (5.36)$$

$$\frac{\partial \eta}{\partial x_g} = \frac{(x - x_g)(x - x_s)r_s + z^2 r_s + r_s^2 r_g}{z r_g r^2} \quad (5.37)$$

$$\left| \frac{\partial(\xi, \eta)}{\partial(x_s, x_g)} \right| = -\frac{2}{(r_s + r_g)^2} = -\frac{2}{r^2} \quad (5.38)$$

$$\left| \frac{\partial(x_s, x_g)}{\partial(\xi, \eta)} \right| = \left(\left| \frac{\partial(\xi, \eta)}{\partial(x_s, x_g)} \right| \right)^{-1} = -\frac{r^2}{2} \quad (5.39)$$

The $M^{Kirchhoff}(x, z, \xi, \eta)$ in equation 5.33 is an algorithm that can provide ray-theory-based angle dependent information from Kirchhoff migration. As shown in figure 5.10, where each red line corresponds to one ξ and each blue line corresponds to one η . If we do not know the dip angle, we can sum along all η (each blue line) to obtain the function $M^{Kirchhoff}(x, z, \xi)$ for each imaging point, and retrieve angle information from

A Comparison of the amplitude properties of two important imaging conditions

this equation. If we know the actual dip angle α_0 and $\eta = \tan\alpha_0$, we can simply select a part of the image $M^{Kirchhoff}(x, z, \xi, \eta = \tan\alpha_0)$ and retrieve angle information from it.

Please understand that while we have provided ray-theory-based angle dependent information for each incident/dip angle subset of the data, that information is now provided over a set of candidate image points. That is in contrast with the uncollapsed Stolt pre-stack migration. Stolt migration(equation 5.8) provides a definite image point and angle dependent information at the image point.

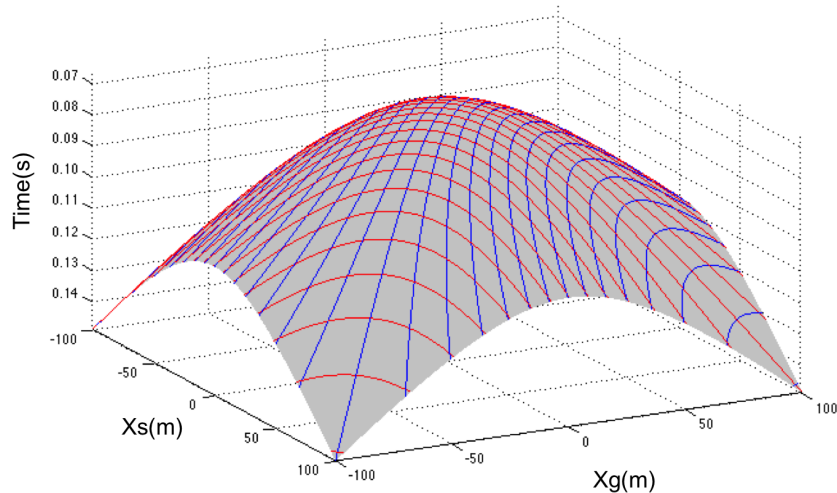


Fig. 5.10: an example of trajectory function $t(x_s, x_g) = r/c$, where each red lines corresponds to one incident angle and each blue line corresponds to one dip angle

5.5 Conclusion

In this chapter we first compared a Claerbout III wave equation migration - Stolt migration and its asymptotic form - Kirchhoff migration. We first studied and tested the effects caused by the stationary phase approximation which has dramatic impact on subsequent imaging steps, and makes the asymptotic migration method not an approximated source and receiver coincident at time equals zero. Then we compared the amplitudes of Stolt migration and Kirchhoff migration for the simplest possible overburden, with both perfect data in the domain each requires, and attempt to retrieve the angle dependent reflection coefficient from both migration methods. For Stolt migration, the retrieved angle dependent reflection coefficient is almost identical as the theoretical value. For Kirchhoff migration, we have two different ways to retrieve the angle dependent reflection coefficient: 1, interpreting the Kirchhoff migration result as a fictitious experiment. 2, using an alternative ray-theory-based algorithm. And in both cases the predicted angle dependent reflection coefficient is not as good as the wave equation migration prediction. The Claerbout III wave equation migration - Stolt migration and its asymptotic form - Kirchhoff migration are quite different. Stolt migration can provide a clear physics meaning with predicting a source and receiver experiment at depth and one can readily obtain the correct angle dependent reflection coefficient. Kirchhoff migration loses the definitive "yes" or "no" to a point being imaged and the ability to provide a correct angle dependent reflection coefficient. And then we compare the single source and receiver image of Kirchhoff migration and RTM, the images indicate that these two migration methods are related.

6. A RESOLUTION COMPARISON BETWEEN RTM AND THE FIRST MIGRATION METHOD THAT IS EQUALLY EFFECTIVE AT ALL FREQUENCIES AT THE TARGET

6.1 Quantify the difference and impact on resolution

To quantify the impact and to examine how different migration methods treat different bandwidths in the data, we examine the relative reduction of side-lobe amplitudes for each migration method using conventional and band-limited data. Side lobes in the data are an expression of the band-limited source. For events in the data, the more we extend the low-frequency content of the spectrum, (1) the smaller the amplitude of side lobes and (2) the closer the side lobes move towards the center of the event.

Fu et al. (2017) produced the first direct comparison of differences in structural resolution produced by RTM (CII) and Stolt extended CIII using data with and without low frequencies and the same homogeneous velocity model. There are two factors that contribute to these differences: (1) the imaging condition itself and (2) the way the imaging condition is implemented. In RTM (CII) both the imaging condition and how the imaging condition is implemented are each separately making high-frequency approximations. In the new imaging method (Stolt extended CIII for heterogeneous media) from M-OSRP both the imaging condition and method of implementation are equally effective at all frequencies at the target and reservoir. There are side lobes in the structural image due to the missing low frequencies. With the new imaging method (see equation 1.3) and including low frequencies in the input data the side lobes are reduced 57% (from 0.33 to 0.14) whereas the

conventional leading edge RTM only reduced the side lobes by 21% (from 0.78 to 0.62). The new imaging method equation 1.3 is able to benefit from broadband data for structural resolution improvement to a much greater extent than the current best industry standard.

In this paper we continue to study the resolution differences of RTM (CII) and Stolt extended CIII. We produce the first wedge-model test for the comparison of structural resolution differences with data with and without low frequencies, using the same homogeneous velocity model, comparing RTM (CII) and Stolt extended CIII. With Stolt extended CIII and including low frequencies in the input data the side lobes are reduced 87% whereas RTM (CII) only reduced the side lobes by 50%. More low frequency was included in these tests than in the earlier Q. Fu et al (2017) tests. This result is consistent with the result in Fu et al. (2017). Stolt extended CIII is able to benefit from broadband data for structural resolution improvement to a much greater extent than the current best industry standard. The wedge model test in this paper further demonstrates that the Stolt extended CIII result has better resolution than the RTM (CII) result due to the smaller side lobes in the image. For Stolt extended CIII broadband data, two reflectors can be identified when the distance between 2 reflectors is greater than 25m, while for RTM (CII) broadband data the distance between 2 reflectors must be greater than 50m. For Stolt extended CIII conventional data, two reflectors can be identified when the distance between 2 reflectors is greater than 50m. while for RTM (CII) conventional data, the distance between 2 reflectors must be greater than 75m.

6.2 Numerical tests on a wedge model

The tests and comparisons in this paper had a broadband data that had a high frequency cut-off but the spectrum was full on the low end. That gave a limit or end-member for the most improvement in resolution for a layer that the new migration equation 1.3 could produce with broadband data. This analysis and conclusion does not depend on having

data down to zero frequency. We generate the two events separately and then combine them together to generate the two-event synthetic data. For each event, a two half-space model is used, the velocity of upper half-space is 1500m/s and the lower one is 2000m/s. For the first events the interface between the two half-space is 1500m. For the second event, the location is varying from 1512.5m to 1275m to mimic the wedge model. The purpose of this procedure is to correctly locate both of the two events in the image space using a homogeneous velocity model.

The two wavelets used in the tests are both band-limited spikes. The frequency range of the first one (broadband) is 0Hz-50Hz and of the other one (conventional) is 20Hz-50Hz. Figure 6.1 (upper left and upper right) shows the frequency spectra of the two wavelets and figure 6.1 (lower left and lower right) shows the time domain waveforms.

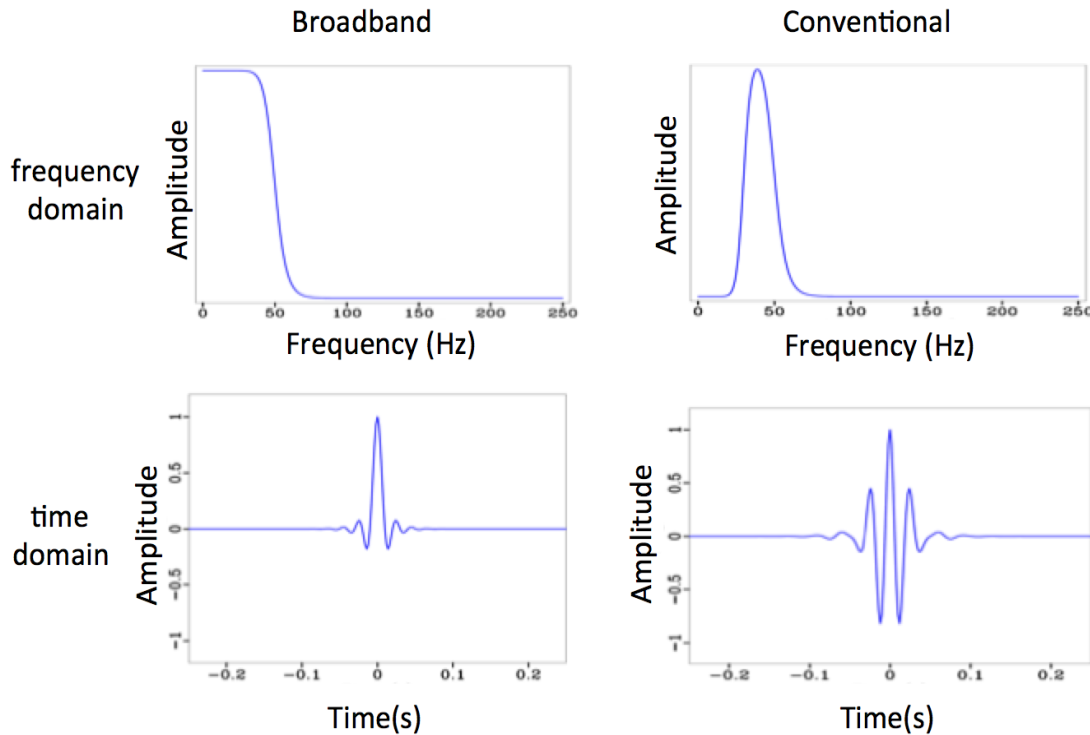


Fig. 6.1: The upper left and upper right show the frequency spectra of the two wavelets; the lower left and lower right show the time-domain waveforms. (The amplitude has no units.)

A Resolution comparison between CII (RTM) and CIII

Figure 6.2 shows the RTM (CII) and Stolt extended CIII images for one reflector at 1500m with the two different wavelets. The upper left is the Stolt extended CIII image with broadband data, the lower left is the Stolt extended CIII image with conventional data, the upper right is the RTM (CII) image with broadband data, and the lower right is the RTM (CII) image with conventional data. For Stolt extended CIII the side lobes are reduced more than 87%, whereas for RTM (CII) the side lobes reduced only about 50%. This result is consistent with that in Q. Fu et al. (2017).

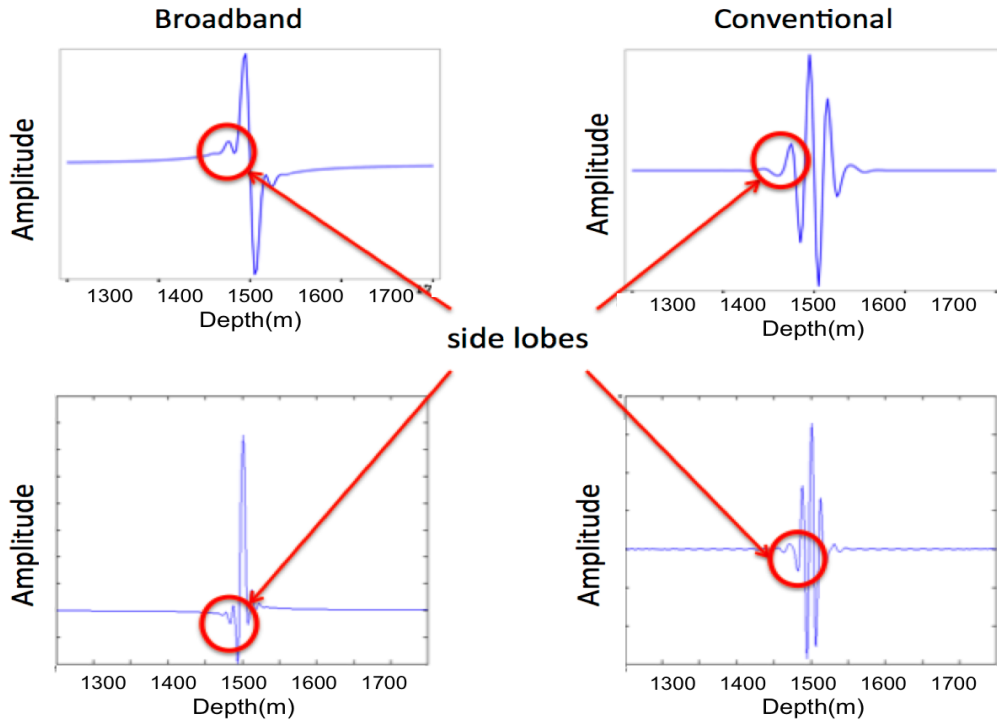


Fig. 6.2: The upper left is the CIII image with broadband data, the lower left is the CIII image with conventional data, the upper right is the RTM (CII) image with broadband data, and the lower right is the RTM (CII) image with conventional data. For CIII the side lobes are reduced more than 87%, whereas for RTM (CII) the side lobes reduced only about 50%. This result is consistent with that in Q. Fu et al. (2017). (The amplitude has no units.)

Figure 6.3-6.6 show the RTM (CII) and Stolt extended CIII image for a wedge model with the broadband data and conventional data. Figure 6.3 shows the Stolt extended CIII wedge model image for broadband data with the first reflector at 1500m and second reflector at

A Resolution comparison between CII (RTM) and CIII

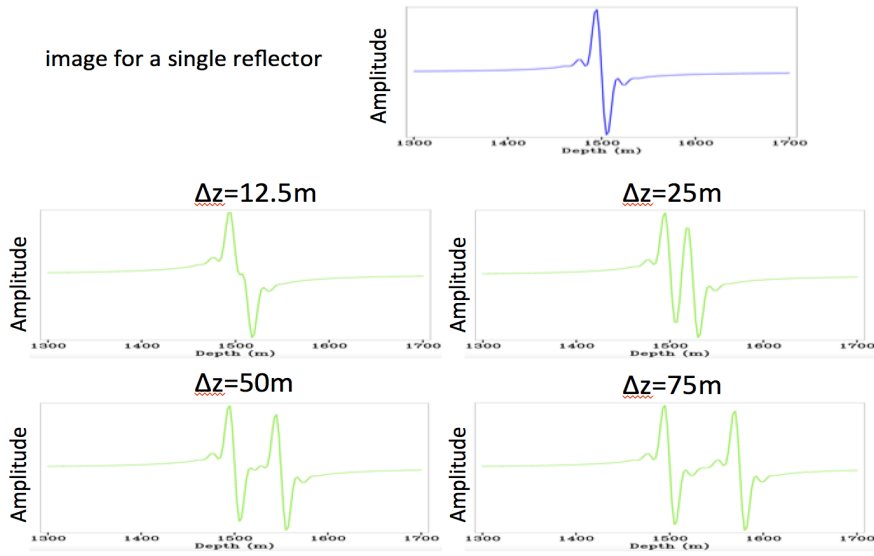


Fig. 6.3: The Stolt extended CIII wedge model image for broadband data with first reflector at 1500m and second reflector at 1512.5m, 1525m, 1550m, 1575m respectively.(The amplitude has no units.)

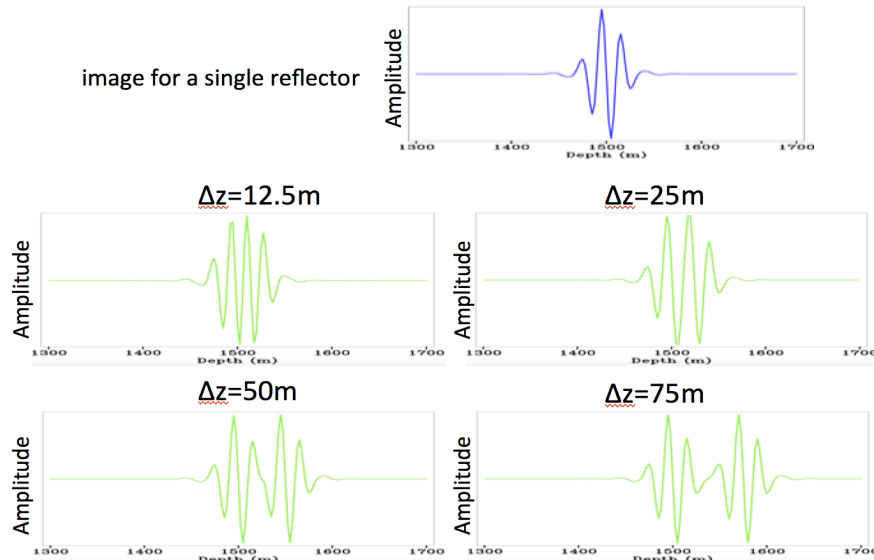


Fig. 6.4: The Stolt extended CIII wedge model image for conventional data with first reflector at 1500m and second reflector at 1512.5m, 1525m, 1550m, 1575m respectively.(The amplitude has no units.)

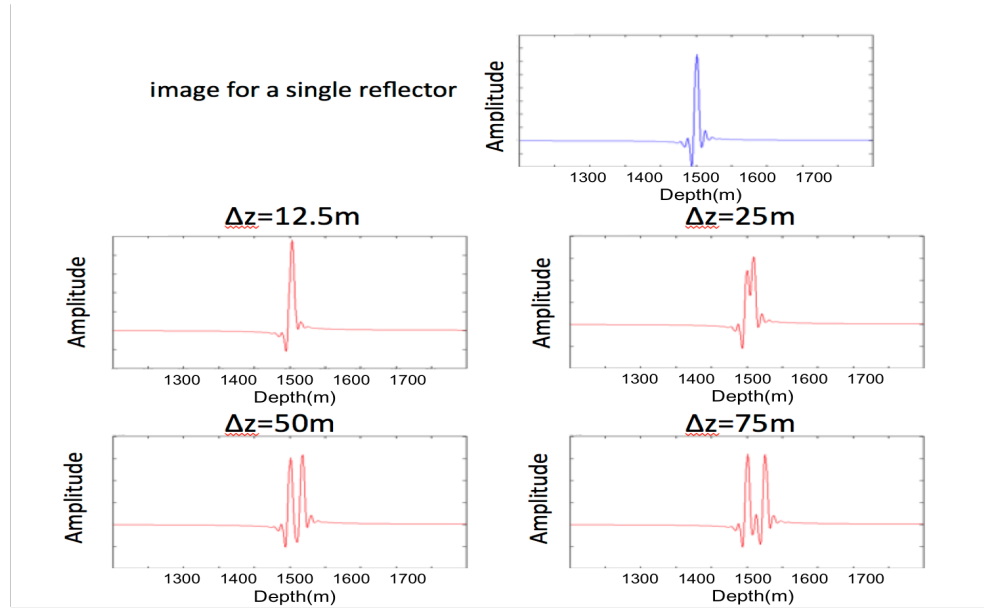


Fig. 6.5: The RTM (CII) wedge model image for broadband data with first reflector at 1500m and second reflector at 1512.5m, 1525m, 1550m, 1575m respectively.(The amplitude has no units.)

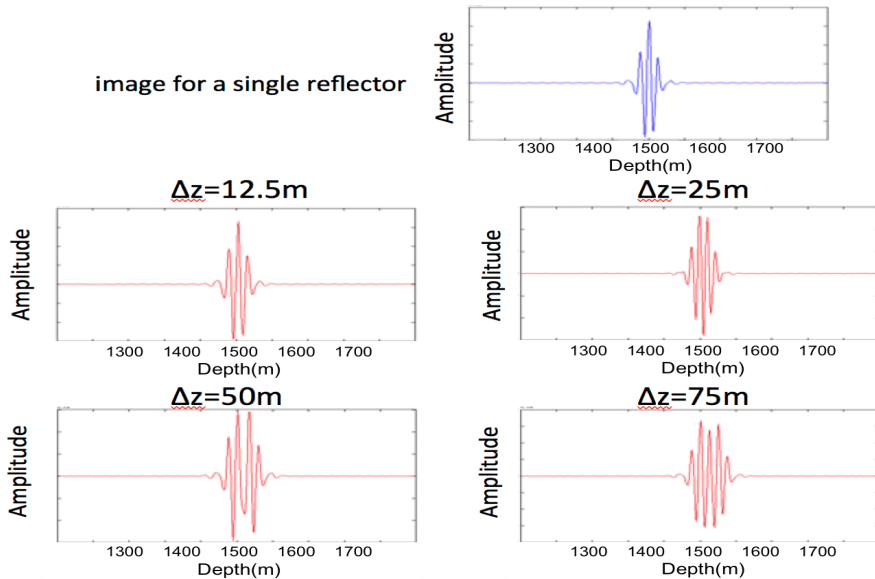


Fig. 6.6: The RTM (CII) wedge model image for conventional data with first reflector at 1500m and second reflector at 1512.5m, 1525m, 1550m, 1575m respectively.(The amplitude has no units.)

A Resolution comparison between CII (RTM) and CIII

1512.5m, 1525m, 1550m, 1575m respectively. Figure 6.4 shows Stolt extended CIII wedge model image for conventional data with first reflector at 1500m and second reflector at 1512.5m, 1525m, 1550m, 1575m respectively. Figure 6.5 shows RTM (CII) wedge model image for broadband data with first reflector at 1500m and second reflector at 1512.5m, 1525m, 1550m, 1575m respectively. Figure 6.6 shows The RTM (CII) wedge model image for conventional data with first reflector at 1500m and second reflector at 1512.5m, 1525m, 1550m, 1575m respectively.

From the figures we can conclude that two reflectors are separated when the distance between 2 reflectors is greater than 25m for Stolt extended CIII Broadband data, 50m for Stolt extended CIII conventional data, 50m for RTM (CII) Broadband data and 75m for RTM (CII) conventional data.

7. CONCLUSION

In the first part of this thesis, we showed the development and evolution of the ISS internal-multiple-elimination algorithm. This algorithm is one part of the three-pronged strategy that is a direct response to current seismic processing and interpretation challenges when primaries and internal multiples are proximal to and/or interfere with each other in both on-shore and off-shore plays. This new algorithm addresses the shortcomings of the current most capable internal-multiple-removal method today used in industry (ISS internal-multiple-attenuation algorithm plus adaptive subtraction). Meanwhile, this elimination algorithm retains the stand-alone benefits of the ISS internal-multiple-attenuation algorithm that can predict all internal multiples at once and requiring no subsurface information (in contrast to stripping and Feedback loop methods that remove multiples layer by layer and require subsurface information). This ISS internal-multiple-elimination algorithm is more effective and more compute-intensive than the current best internal-multiple-removal method. Within the three-pronged strategy ((1) Provide the prerequisites for ISS multiple removal methods for on-shore applications.(2) Develop internal-multiple elimination algorithms from ISS. (3) Develop a replacement for the energy-minimization criteria for adaptive subtraction that derives from and always aligns with the ISS elimination algorithm.), our plans include developing an alternative adaptive-subtraction criteria for internal-multiple elimination derived from, and always aligned with the ISS elimination algorithm. That would be analogous to the new adaptive criteria for free-surface-multiple removal proposed by Weglein (2012), as a replacement for the energy-minimization criteria for adaptive subtraction. We provide this new multi-dimensional internal-multiple-elimination method as a

Conclusion

new internal-multiple-removal capability in the multiple-removal toolbox that can remove internal multiples that interfere with primaries without subsurface information and without damaging the primary. In the development of current elimination algorithm, we assumed an acoustic relationship $T = 1+R$ between transmission coefficients T and reflection coefficients R. In the future, we will develop a model-type independent internal-multiple elimination algorithm that can more effectively accommodates an elastic and inelastic subsurface.

In the second part of this thesis, we produced the first wedge-model test for the comparison of structural resolution differences with data with and without low frequencies, comparing the current leading edge RTM (CII) and the Stolt extended CIII imaging principle. RTM (CII) has a high-frequency assumption in its imaging principle. The Stolt extended CIII imaging principle is not a high-frequency imaging principle. There are side lobes in the structural image due to the missing low frequencies. For a single reflector, including low frequencies in the input data, the side lobes are reduced 87% in Stolt extended CIII whereas the side lobes are only reduced 50% in RTM (CII), which is consistent with the result in Q. Fu et al. (2017). The new CIII imaging method is able to benefit from broadband data for structural resolution improvement to a much greater extent than the current best industry standard migration. The wedge model test further demonstrates that the Stolt extended CIII result has better resolution than the RTM (CII) result due to the smaller side lobes in the image from each reflector. For Stolt extended CIII with broadband data, two reflectors can be identified when the distance between 2 reflectors is greater than 25m, while for RTM (CII) with broadband data the distance between 2 reflectors must be greater than 50m. For Stolt extended CIII with conventional data, two reflectors can be identified when the distance between 2 reflectors is greater than 50m, while for RTM (CII) with conventional data, the distance between 2 reflectors must be greater than 75m.

Furthermore, all current migration methods (including RTM) assume a one-way propagation model at every point in the subsurface for a smooth velocity model. That one-way

Conclusion

propagation model is a high-frequency approximation. The new Stolt extended CIII for heterogeneous media assumes a two-way propagation model at every point in a smoothly varying medium. The next planned tests will include implementation differences (i.e. the wave propagation component of migration) for a smooth velocity model. The differences in resolution derived from the new migration method, Stolt extended CIII for heterogeneous media, that makes no high-frequency approximation in both (A) the wave propagation concept (B) the imaging principle will be greater when both the imaging principle and the wave propagation model are included than we report here for only the imaging principle differences.

APPENDIX

A. ATTENUATION FACTOR IN ACOUSTIC AND ELASTIC MEDIUM

In this thesis, we develop the acoustic internal-multiple elimination algorithm based on the relationship $T=1+R$ between reflection coefficients and transmission coefficients. Much of the analytic example is for acoustic medium. The relationship of $T=1+R$ does not hold for elastic medium due to converted waves. The following figure A.1 shows the attenuation factor for an acoustic two reflector model and an elastic two reflector model. For the acoustic model, above the reflector $V = 1500m/s$, $\rho = 1.0 \times 10^3 m^3/kg$, below the reflector $V = 2000m/s$, $\rho = 2.0 \times 10^3 m^3/kg$. For the elastic model, above the reflector $V_p = 1500m/s$, $V_s = 500m/s$, $\rho = 1.0 \times 10^3 m^3/kg$, below the reflector $V_p = 2000m/s$, $V_s = 700m/s$, $\rho = 2.0 \times 10^3 m^3/kg$. The figures shows the attenuation factor for acoustic and elastic medium are close especially for small incident angles.

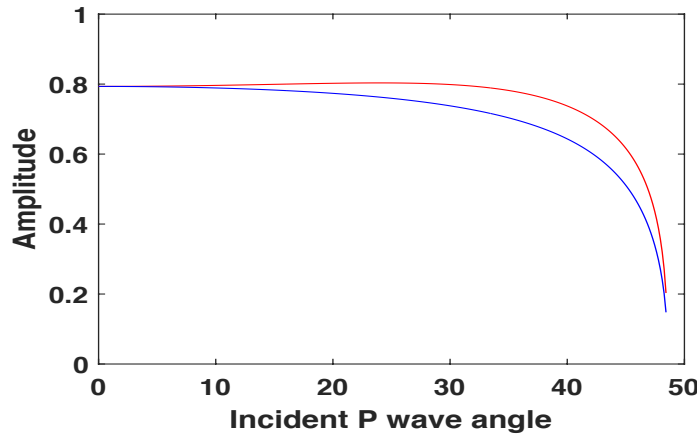


Fig. A.1: Acoustic and elastic attenuation factor, red line is the attenuation factor for acoustic medium, blue line is the attenuation factor for elastic medium (The amplitude does not have units.)

B. DERIVATION OF THE ALGORITHM FOR THE ELIMINATION OF ALL FIRST-ORDER INTERNAL MULTIPLES FROM ALL REFLECTORS IN A 1D MEDIUM

The middle part of the 1D normal incidence algorithm is:

$$F[b_1(z)] = \frac{b_1(z)}{[1 - (\int_{z-\varepsilon}^{z+\varepsilon} dz' g(z'))^2][1 - \int_{-\infty}^{z-\varepsilon} dz' b_1(z') \int_{z'-\varepsilon}^{z'+\varepsilon} dz'' g(z'')]^2] \quad (B.1)$$

$$g(z) = \frac{b_1(z)}{1 - \int_{-\infty}^{z-\varepsilon} dz' b_1(z') \int_{z'-\varepsilon}^{z'+\varepsilon} dz'' g(z'')} \quad (B.2)$$

$(\int_{z-\varepsilon}^{z+\varepsilon} dz'' g(z'')$ is a function of z)

Consider a data with n primaries, we have

$$b_1(z) = R_1 \delta(z - z_1) + R'_2 \delta(z - z_2) + R'_3 \delta(z - z_3) + \cdots + R'_n \delta(z - z_n) + \cdots \quad (B.3)$$

$$g(z) = R_1 \delta(z - z_1) + R_2 \delta(z - z_2) + R_3 \delta(z - z_3) + \cdots + R_n \delta(z - z_n) + \cdots \quad (B.4)$$

Next we will show that the F function actually removed the attenuation factor in the prediction.

Appendix

First Let's calculate $\int_{z-\varepsilon}^{z+\varepsilon} dz'' g(z'')$ for the given $g(z)$:

$$\begin{aligned}
\int_{z-\varepsilon}^{z+\varepsilon} dz'' g(z'') &= \int_{z-\varepsilon}^{z+\varepsilon} dz'' [R_1 \delta(z'' - z_1) + R_2 \delta(z'' - z_2) + \cdots + R_n \delta(z'' - z_n) + \cdots] \\
&= \int_{-\infty}^{\infty} dz'' [R_1 \delta(z'' - z_1) + R_2 \delta(z'' - z_2) + \cdots + R_n \delta(z'' - z_n) + \cdots] \\
&\quad \times H(z'' - (z - \varepsilon)) H((z + \varepsilon) - z'') \\
&= R_1 H(z_1 - (z - \varepsilon)) H((z + \varepsilon) - z_1) + R_2 H(z_2 - (z - \varepsilon)) H((z + \varepsilon) - z_2) \\
&\quad + \cdots + R_n H(z_n - (z - \varepsilon)) H((z + \varepsilon) - z_n) + \cdots \\
&= R_1 H((z_1 + \varepsilon) - z) H(z - (z_1 - \varepsilon)) + R_2 H((z_2 + \varepsilon) - z) H(z - (z_2 - \varepsilon)) \\
&\quad + \cdots + R_n H((z_n + \varepsilon) - z) H(z - (z_n - \varepsilon)) + \cdots \tag{B.5}
\end{aligned}$$

$$\begin{aligned}
&(\int_{z-\varepsilon}^{z+\varepsilon} dz'' g(z''))^2 \\
&= R_1^2 H((z_1 + \varepsilon) - z) H(z - (z_1 - \varepsilon)) + R_2^2 H((z_2 + \varepsilon) - z) H(z - (z_2 - \varepsilon)) \\
&\quad + \cdots + R_n^2 H((z_n + \varepsilon) - z) H(z - (z_n - \varepsilon)) + \cdots \tag{B.6}
\end{aligned}$$

$$\begin{aligned}
&b_1(z') \int_{z'-\varepsilon}^{z'+\varepsilon} dz'' g(z'') \\
&= R_1^2 \delta(z' - z_1) + R_2 R'_2 \delta(z' - z_2) + R_3 R'_3 \delta(z' - z_3) + \cdots + R_n R'_n \delta(z' - z_n) + \cdots \tag{B.7}
\end{aligned}$$

Appendix

$$\begin{aligned}
& \int_{-\infty}^{z-\varepsilon} dz' b_1(z') \int_{z'-\varepsilon}^{z'+\varepsilon} dz'' g(z'') \\
&= \int_{-\infty}^{z-\varepsilon} dz' [R_1^2 \delta(z' - z_1) + R_2 R'_2 \delta(z' - z_2) + \cdots + R_n R'_n \delta(z' - z_n) + \cdots] \\
&= \int_{-\infty}^{\infty} dz' H((z - \varepsilon) - z') [R_1^2 \delta(z' - z_1) + R_2 R'_2 \delta(z' - z_2) + \cdots + R_n R'_n \delta(z' - z_n) + \cdots] \\
&= R_1^2 H((z - \varepsilon) - z_1) + R_2 R'_2 H((z - \varepsilon) - z_2) + \cdots + R_n R'_n H((z - \varepsilon) - z_n) + \cdots \\
&= R_1^2 H(z - (z_1 + \varepsilon)) + R_2 R'_2 H(z - (z_2 + \varepsilon)) + \cdots + R_n R'_n H(z - (z_n + \varepsilon)) + \cdots \quad (\text{B.8})
\end{aligned}$$

Now we can prove the first part of the equation:

$$\begin{aligned}
& F[b_1(z)] \\
&= \frac{b_1(z)}{[1 - (\int_{z-\varepsilon}^{z+\varepsilon} dz' g(z'))^2][1 - \int_{-\infty}^{z-\varepsilon} dz' b_1(z') \int_{z'-\varepsilon}^{z'+\varepsilon} dz'' g(z'')]^2} \\
&= \frac{b_1(z)}{[1 - R_1^2 H((z_1 + \varepsilon) - z) H(z - (z_1 - \varepsilon)) - \cdots]} \\
&\quad \times \frac{1}{[1 - R_1^2 H(z - (z_1 + \varepsilon)) - R_2 R'_2 H(z - (z_2 + \varepsilon)) - \cdots]^2} \\
&= \frac{R_1}{1 - R_1^2} \delta(z - z_1) + \frac{R'_2}{(1 - R_1^2)^2 (1 - R_2^2)} \delta(z - z_2) + \cdots \\
&\quad + \frac{R'_n}{(1 - R_1^2)^2 (1 - R_2^2)^2 \cdots (1 - R_{n-1}^2)^2 (1 - R_n^2)} \delta(z - z_n) + \cdots \\
&= \frac{R_1}{AF_{j=1}} \delta(z - z_1) + \frac{R'_2}{AF_{j=2}} \delta(z - z_2) + \cdots + \frac{R'_n}{AF_{j=n}} \delta(z - z_n) + \cdots \quad (\text{B.9})
\end{aligned}$$

For the second part of the equation:

$$g(z) = \frac{b_1(z)}{1 - \int_{-\infty}^{z-\varepsilon} dz' b_1(z') \int_{z'-\varepsilon}^{z'+\varepsilon} dz'' g(z'')} \quad (\text{B.10})$$

Appendix

$$\begin{aligned}
& b_1(z') \int_{z'-\varepsilon}^{z'+\varepsilon} dz'' g(z'') \\
& = R_1^2 \delta(z' - z_1) + R_2 R'_2 \delta(z' - z_2) + R_3 R'_3 \delta(z' - z_3) + \cdots + R_n R'_n \delta(z' - z_n) + \cdots \quad (\text{B.11})
\end{aligned}$$

$$\begin{aligned}
& \int_{-\infty}^{z-\varepsilon} dz' b_1(z') \int_{z'-\varepsilon}^{z'+\varepsilon} dz'' g(z'') \\
& = \int_{-\infty}^{z-\varepsilon} dz' [R_1^2 \delta(z' - z_1) + R_2 R'_2 \delta(z' - z_2) + \cdots + R_n R'_n \delta(z' - z_n) + \cdots] \\
& = \int_{-\infty}^{\infty} dz' H((z - \varepsilon) - z') [R_1^2 \delta(z' - z_1) + R_2 R'_2 \delta(z' - z_2) + \cdots + R_n R'_n \delta(z' - z_n) + \cdots] \\
& = R_1^2 H((z - \varepsilon) - z_1) + R_2 R'_2 H((z - \varepsilon) - z_2) + \cdots + R_n R'_n H((z - \varepsilon) - z_n) + \cdots \\
& = R_1^2 H(z - (z_1 + \varepsilon)) + R_2 R'_2 H(z - (z_2 + \varepsilon)) + \cdots + R_n R'_n H(z - (z_n + \varepsilon)) + \cdots \quad (\text{B.12})
\end{aligned}$$

$$\begin{aligned}
& \frac{b_1(z)}{1 - \int_{-\infty}^{z-\varepsilon} dz' b_1(z') \int_{z'-\varepsilon}^{z'+\varepsilon} dz'' g(z'')} \\
& = R_1 \delta(z - z_1) + \frac{R'_2}{1 - R_1 R_1} \delta(z - z_2) + \frac{R'_3}{1 - R_1 R_1 - R'_2 R_2} \delta(z - z_3) + \cdots \\
& \quad + \frac{R'_n}{1 - R_1 R_1 - R'_2 R_2 - \cdots - R'_{n-1} R_{n-1}} \delta(z - z_n) \\
& = R_1 \delta(z - z_1) + R_2 \delta(z - z_2) + R_3 \delta(z - z_3) + \cdots + R_n \delta(z - z_n) + \cdots \\
& = g(z) \quad (\text{B.13})
\end{aligned}$$

Thus the second equation is proved.

Appendix

In the derivation we used: $R_i = \frac{R'_i}{1 - R_1 R_1 - R'_2 R_2 - \cdots - R'_{i-1} R_{i-1}}$ It can be proved:

$$\begin{aligned}
R_i &= \frac{R'_i}{(1 - R_1^2)(1 - R_2^2) \cdots (1 - R_{i-2}^2)(1 - R_{i-1}^2)} \\
&= \frac{R'_i}{(1 - R_1^2)(1 - R_2^2) \cdots (1 - R_{i-2}^2) - (1 - R_1^2)(1 - R_2^2) \cdots (1 - R_{i-2}^2) R_{i-1}^2} \\
&= \frac{R'_i}{(1 - R_1^2)(1 - R_2^2) \cdots (1 - R_{i-2}^2) - (1 - R_1^2)(1 - R_2^2) \cdots (1 - R_{i-2}^2) R_{i-1}} \\
&= \frac{R'_i}{(1 - R_1^2)(1 - R_2^2) \cdots (1 - R_{i-2}^2) - R'_{i-1} R_{i-1}} \\
&= \frac{R'_i}{1 - R_1 R_1 - R'_2 R_2 - \cdots - R'_{i-1} R_{i-1}}
\end{aligned} \tag{B.14}$$

C. FOURIER TRANSFORM OF THE DATA FROM THE FREQUENCY-SPACE DOMAIN TO THE FREQUENCY-WAVENUMBER DOMAIN

$$D(x_s, x_g, \omega) = \frac{1}{2\pi} \int_{-\omega/c}^{\omega/c} dk'_s \frac{e^{-ik'_s x_s}}{2iq'_s} R(k'_s, q'_s) e^{ik'_s x_g} e^{2iq'_s z_1} \quad (\text{C.1})$$

$$\begin{aligned} D(k_s, x_g, \omega) &= \frac{1}{2\pi} \int_{-\infty}^{\infty} dx_s e^{ik_s x_s} \int_{-\omega/c}^{\omega/c} dk'_s \frac{e^{-ik'_s x_s}}{2iq'_s} R(k'_s, q'_s) e^{ik'_s x_g} e^{2iq'_s z_1} \\ &= \frac{1}{2\pi} \int_{-\omega/c}^{\omega/c} \int_{-\infty}^{\infty} dx_s e^{i(k_s - k'_s)x_s} dk'_s \frac{R(k'_s, q'_s) e^{ik'_s x_g} e^{2iq'_s z_1}}{2iq'_s} \\ &= \frac{1}{2\pi} \int_{-\omega/c}^{\omega/c} dk'_s \delta(k_s - k'_s) \frac{R(k'_s, q'_s) e^{ik'_s x_g} e^{2iq'_s z_1}}{2iq'_s} \\ &= \frac{R(k_s, q_s) e^{ik_s x_g} e^{2iq_s z_1}}{4\pi iq_s} (-\omega/c < k_s < \omega/c) \end{aligned} \quad (\text{C.2})$$

$$\begin{aligned} D(k_s, k_g, \omega) &= \int_{-\infty}^{\infty} dx_g e^{-ik_g x_g} \frac{R(k_s, q_s) e^{ik_s x_g} e^{2iq_s z_1}}{4\pi iq_s} (-\omega/c < k_s < \omega/c) \\ &= \delta(k_s - k_g) \frac{R(k_s, q_s) e^{2iq_s z_1}}{4\pi iq_s} (-\omega/c < k_s < \omega/c) \end{aligned} \quad (\text{C.3})$$

D. SYNTHETIC DATA GENERATION BY CAGNIARD-DE HOOP METHOD

For one reflector model, the analytic data can be calculated by Cagniard-de Hoop method in space-time domain (as utilized in Zhang and Weglein (2006)). In an acoustic medium, for a source at (x_s, z_s) , and a receiver at (x_g, z_g) , the pre-critical reflection data is

$$P(x_s, x_g, z_s, z_g, t) = \frac{1}{2\pi} \text{Re}(\widehat{pp}) \frac{H(t - r/c_0)}{\sqrt{t - r^2/c_0^2}}, \quad (\text{D.1})$$

with

$$r = \sqrt{(x_s - x_g)^2 + (z_s + z_g - 2z_r)^2}, \quad (\text{D.2})$$

where z_r is the depth of the reflector, c_0 is the velocity in the first layer and t is the recorded time.

E. SYNTHETIC DATA GENERATION BY REFLECTIVITY METHOD

For 1D earth, the analytic data can be calculated by the reflectivity method in the frequency-wave number domain, e.g., in Ewing et al. (1957). For one reflector in an acoustic medium, assuming the a source and a receiver are located at $(x_s, 0)$ and $(x_g, 0)$ respectively, the data can be calculated as

$$\begin{aligned} D(k_{sx}, k_{gx}, \omega) &= \int_{-\infty}^{+\infty} dx_g e^{-ik_{gx}x_g} \frac{r(k_{sx}, k_{sz}) e^{ik_{sx}x_g} e^{2ik_{sz}z_r}}{4\pi i q_s} \\ &= \delta(k_{sx} - k_{gx}) \frac{r(k_{sx}, k_{sz}) e^{2ik_{sz}z_r}}{4\pi i k_{sz}}. \end{aligned} \quad (\text{E.1})$$

where k_{sx} and k_{gx} are the Fourier transform of x_s and x_g respectively, k_{gx} is defined in the same way in Section 2, ω is the temporal frequency and z_r is the depth of the reflector.

BIBLIOGRAPHY

- Araújo, F. V. *Linear and non-linear methods derived from scattering theory: backscattered tomography and internal multiple attenuation.* PhD thesis, Universidade Federal da Bahia, 1994.
- Araújo, F. V., A. B. Weglein, P. M. Carvalho, and R. H. Stolt. “Inverse scattering series for multiple attenuation: An example with surface and internal multiples.” *SEG Technical Program Expanded Abstracts* (1994): 1039–1041.
- Claerbout, Jon F. “Toward a unified theory of reflector mapping.” *Geophysics* 36 (June 1971): 467–481.
- Clayton, R. W. and R. H. Stolt. “A Born-WKBJ inversion method for acoustic reflection data.” *Geophysics* 46 (1981): 1559–1567.
- Ewing, W. M., W. S. Jardetzky, and F. Press. *Elastic waves in layered media.* McGraw-Hill Book Co., 1957.
- Fu, Qiang, Yanglei Zou, and Arthur B. Weglein. “An initial study to quantify the resolution difference between an industry leading-edge migration, RTM, and the first migration method that is equally effective at all frequencies at the target.” *87th Annual International Meeting, SEG, Expanded Abstracts.* Submitted, 2017.
- H. Liang, C. Ma and A. B. Weglein. “A further general modification of the leading order ISS attenuator of first-order internal multiples to accommodate primaries and internal

Bibliography

- multiples when an arbitrary number of reflectors generate the data: theory, development, and examples.” *Mission Oriented Seismic Research Program Annual Report* (2012): 148–165.
- Herrera, Hong Liang Paolo Terenghi, Chao Ma and Arthur B. Weglein. “Progressing amplitude issues for testing 1D analytic data in leading order internal multiple algorithms.” *Mission Oriented Seismic Research Program Annual Report* (2012): 167–188.
- Lecerf, D., E. Hodges, S. Lu, A. Valenciano, N. Chemingui, P. Johann, and E. Thedy. “Imaging primaries and high-order multiples for permanent reservoir monitoring: Application to Jubarte field.” *The Leading Edge* 34 (2015): 824–826, 828–828.
- Liu, Fang. The first wave theory RTM, examples with a layered medium, predicting the source and receiver at depth and then imaging, providing the correct location and reflection amplitude at every depth location, and where the data includes primaries and all internal multiples. Presentation given at the 2013 M-OSRP Annual Meeting, available online at mosrp.uh.edu, May 2013.
- Lowenthal, D., L. Lu, R. Roberson, and J. W. C. Sherwood. “The wave equation applied to migration.” *Geophysical Prospecting* 24 (1985): 380–399.
- Lu, S., N.D. Whitmore, A.A. Valenciano, N. Chemingui, and G. Rnholt. “A practical crosstalk attenuation method for separated wavefield imaging.” *SEG Expanded Abstracts*. (2016).
- Ma, C., H. Liang, and A. B. Weglein. “Modifying the leading order ISS attenuator of first-order internal multiples to accommodate primaries and internal multiples: fundamental concept and theory, development, and examples exemplified when three reflectors generate the data.” *Mission Oriented Seismic Research Program Annual Report* (2012): 133–147.

Bibliography

- Ma, C. and A. B. Weglein. “Including higher-order Inverse Scattering Series (ISS) terms to address a serious shortcoming/problem of the ISS internal-multiple attenuator: exemplifying the problem and its resolution.” *SEG Technical Program Expanded Abstracts* (2014).
- Nita, B. G., K. H. Matson, and A. B. Weglein. “Forward scattering series and seismic events: Far field approximations, critical and postcritical events.” *SIAM Journal of Applied Mathematics* 64 (2004): 2167–2185.
- Ramírez, A. C. *1.-Inverse scattering subseries for removal of internal multiples and depth imaging primaries; 2.-Green’s theorem as the foundation of interferometry and guiding new practical methods and applications*. PhD thesis, University of Houston, 2007.
- Riley, D. C. and J. F. Claerbout. “2D multiple reflections.” *Geophysics* 41 (1976): 592–620.
- Shen, Yuchang. and A. B. Weglein. “Impact of the shape of the acquisition surface on the effectiveness of the ISS internal multiple attenuation and elimination algorithms: analyzing the problem and providing a response to the challenge.” *MOSRP annual report* (2017).
- Stolt, R. H. “Migration by Fourier transform.” *Geophysics* 43 (1978): 23–48.
- Stolt, R. H. and A. B. Weglein. “Migration and inversion of seismic data.” *Geophysics* 50 (1985): 2458–2472.
- Stolt, Robert H. and Alvin K. Benson. *Seismic migration: theory and practice*. London—Amsterdam: Geophysical Press, 1986.
- Stolt, Robert H. and Arthur B. Weglein. *Seismic Imaging and Inversion: Application of Linear Inverse Theory*. Cambridge University Press, February 2012.
- Valenciano, A. and N. Chemingui. “Introduction to this special section: Multiples from attenuation to imaging.” *The Leading Edge* 34 (2015): 742–742.

Bibliography

- Weglein, A. B., F. V. Araújo, P. M. Carvalho, R. H. Stolt, K. H. Matson, R. T. Coates, D. Corrigan, D. J. Foster, S. A. Shaw, and H. Zhang. “Inverse Scattering Series and Seismic Exploration.” *Inverse Problems* (2003): R27–R83.
- Weglein, A. B., F. A. Gasparotto, P. M. Carvalho, and R. H. Stolt. “An Inverse-Scattering Series Method for Attenuating Multiples in Seismic Reflection Data.” *Geophysics* 62 (November-December 1997): 1975–1989.
- Weglein, A. B. and K. H. Matson. “Inverse Scattering Internal Multiple Attenuation: An Analytic Example and Subevent interpretation.” *SPIE Conference on Mathematical Methods in Geophysical Imaging*. 1998, 108–117.
- Weglein, A. B. and R. H. Stolt. “Migration-Inversion Revisited.” *The Leading Edge* Aug (1999): 950.
- Weglein, A. B., R. H. Stolt, and J. D. Mayhan. “Reverse-time migration and Green’s theorem: Part I — The evolution of concepts, and setting the stage for the new RTM method.” *Journal of Seismic Exploration* 20 (February 2011): 73–90.
- Weglein, A. B., R. H. Stolt, and J. D. Mayhan. “Reverse time migration and Green’s theorem: Part II — A new and consistent theory that progresses and corrects current RTM concepts and methods.” *Journal of Seismic Exploration* 20 (May 2011): 135–159.
- Weglein, Arthur, James Mayhan, Yanglei Zou, Qiang Fu, Fang Liu, Jing Wu, Chao Ma, Xinglu Lin, and Robert Stolt. “The first migration method that is equally effective for all acquired frequencies for imaging and inverting at the target and reservoir.” *86th Annual International Meeting, SEG, Expanded Abstracts*. 2016, 4266–4272.
- Weglein, Arthur B. “Multiple attenuation: The status and a strategy that identifies and addresses current challenges.” (2014).

Bibliography

Weglein, Arthur B. "Multiples: signal or noise?." *84th Annual International Meeting, SEG, Expanded Abstracts*. Submitted, 2014.

Wu, Jing. and A. B. Weglein. "A new method for deghosting data collected on a depth-variable acquisition surface by combining Greens theorem wave separation followed by a Greens theorem wave prediction for one-way propagating waves." *MOSRP annual report* (2017).

Zhang, Jingfeng and Arthur B. Weglein. "A note on data modelling using the Cagniard-de Hoop method." *M-OGRP 2005-2006 Annual Report*. 2006, 126–138.

Zhang, Zhen. and A. B. Weglein. "3D source and receiver deghosting in the space-frequency domain using a depthvariable measurement surface: an initial off-shore synthetic data study with anticipated on-shore and ocean bottom application." *MOSRP annual report* (2017).

Zou, Yanglei., Chao. Ma, and A. B. Weglein. "The first Inverse-Scattering-Series internal multiple elimination method for a multi-dimensional subsurface." *MOSRP annual report* (2016).

Zou, Yanglei. and A. B. Weglein. "An internal-multiple elimination algorithm for all reflectors for 1D earth Part I: Strengths and limitations." *Journal of Seismic Exploration* (2014).